The Astronomical Journal, 127:606–624, 2004 February

JET-GAS INTERACTIONS IN MARKARIAN 78. I. MORPHOLOGY AND KINEMATICS

Mark Whittle
Department of Astronomy, University of Virginia, Charlottesville, VA 22903; dmw8f@virginia.edu

and

Andrew S. Wilson[1]
Department of Astronomy, University of Maryland, College Park, MD 20742; wilson@astro.umd.edu
Received 2002 August 28; accepted 2003 October 22

ABSTRACT

We present a detailed study of the Seyfert 2 galaxy Markarian 78, using continuum and emission-line images and multiaperture spectra from the *Hubble Space Telescope* (*HST*) and a deep 3.6 cm VLA image. Our overall aim is to study the interaction between the radio source and the emission-line gas, since ground-based data already indicate the presence of a strong bipolar jet-driven flow. First, in the wider context, Mrk 78 is probably a post-merger system, with a nuclear dust lane, approximate $r^{1/4}$ continuum profile, and highly extended asymmetric gas distribution. The [O III] and radio images both show complex structures with many similarities but also important differences. A careful comparison shows convincing *morphological* evidence for jet-gas interaction: (1) the western inner radio jet terminates and flares at the position of a bright [O III] knot; (2) the weaker eastern radio jet changes direction as it encounters a large [O III] knot; (3) most [O III] features appear limb brightened on the upstream side, and flared on the downstream side; and (4) in the outer regions the radio components tend to lie between or adjacent to [O III] knots, indicating the radio and line emitting phases do not easily interpenetrate. In addition to evidence of jet-gas interaction, two features indicate the importance of a central ionizing radiation field: an inner fanlike structure to the east, with a straight kinematically quiet northern edge; and an approximately fanlike extended narrow-line region to the west, lying well outside the radio source. The [O III] line profiles from 10 Faint Object Spectrograph apertures provide further *kinematic* insight into the jet-gas interaction. (1) On the eastern side, where the radio source is deflected, the [O III] profile contains a highly redshifted component ($\sim$700 km s^{-1}) that is also *narrow* (FWHM $\leq$ 200 km s^{-1}), indicating significant coherent gas acceleration with almost no induced turbulence. (2) At this location, the [O III] profile is also double, suggesting lateral expansion away from a jet axis, as it burrows into the cloud complex. (3) In contrast, the bright western inner knot, which seems to disrupt the inner radio jet, has essentially undisturbed kinematics. (4) Across the outer complex western region, gas velocities are higher in the region center, decrease at the leading edge and may be highest where radio flows "blow out" of the region. Overall, morphology and kinematics suggest the western side is best described as an initially disrupted jet that then fills, accelerates, and leaks out of a complex incomplete "bubble" of ionized gas. The eastern side is best described as a large centrally illuminated fanlike gas structure that is penetrated, accelerated, and ultimately deflects the radio source. We use these different regions to construct a plausible evolutionary sequence: Initially, a dense (molecular?) cloud enters the jet flow and disrupts it (inner western knot); as time passes, the jet begins to penetrate, accelerate, and ablate the cloud (eastern knot complex); continued jet influence further disperses the cloud fragments, sweeping out channels and gaps (western lobe region). This process may repeat itself many times over the lifetime of the jet. In companion papers, we study the ionization mechanisms and jet properties in more detail using recently acquired Space Telescope Imaging Spectrograph spectra, taking a more complete account of the energetics of the radio source and the ionized gas.

Key words: galaxies: individual (Markarian 78) — galaxies: jets — galaxies: kinematics and dynamics — galaxies: Seyfert — ISM: jets and outflows

1. INTRODUCTION

An important and astrophysically rich theme in the study of active galaxies is the interaction between the radio-emitting flows and the line-emitting gas. This "jet-gas interaction" can occur in a wide range of circumstances—from near-nuclear to intergalactic environments, at low or high radio power, and at low or high redshift. The physical phenomena encountered are also very varied—radio jets can be disrupted or deflected, they can ablate, shock, accelerate, or destroy line-emitting clouds, and they can even trigger star formation. Not surprisingly, therefore, examples of jet-gas interaction have become a major research focus, increasingly so since the *Hubble Space Telescope* (*HST*) now gives access to the subarsecond structures that characterize many systems. However, finding a clean example to study is not easy, since in most cases either unrelated emission or raw complexity confuses the nature of the interaction. We have therefore chosen to study in detail one of the strongest and cleanest examples of a jet-gas interaction: Markarian 78.

Before considering jet-gas interactions, it is appropriate to place this topic in a broader context. For Seyfert narrow-line

[1] Adjunct astronomer, Space Telescope Science Institute, which is operated by the Association of Universities for Research in Astronomy, Inc., under NASA contract NAS 2-26555.

regions (NLRs), the principal kinematic component is a gravitational one, with line widths matching bulge gravitational velocities (e.g., Whittle 1985a; Wilson & Heckman 1985; Whittle 1992c; Nelson & Whittle 1996). Only in the minority of Seyferts with relatively luminous linear radio sources is there evidence for significant additional (jet-related) acceleration. Even the ubiquitous extended blue wings on [O III] profiles show little correlation with radio properties and may therefore be unrelated to the radio source (Heckman et al. 1981; Whittle 1985b). Thus, even when jet-gas interactions are important, they may be only one of several ongoing processes.

Nevertheless, the evidence for a more general relationship between radio sources and emission-line regions in Seyferts is widespread. Early comparison of emission-line and radio images showed similar sizes (de Bruyn & Wilson 1978) and orientations (e.g., Haniff, Wilson, & Ward 1988), while more recent *HST*/VLA/MERLIN comparisons often reveal quite detailed morphological correspondence (e.g., Bower et al. 1994; Mulchaey et al. 1994; Capetti et al. 1996; Galimore, Baum, & O'Dea 1996; Falcke, Wilson, & Simpson 1998; Schmitt et al. 2003). Early kinematic evidence for jet-gas interactions includes the correlation between [O III] line width and radio luminosity (Wilson & Willis 1980; Wilson 1982) and the tendency for Seyferts with luminous linear radio sources to have supervirial line widths, as well as high-velocity features close to radio lobes (Whittle et al. 1988; Whittle 1992b). Since then, a number of groups have published detailed studies of individual Seyferts with signatures of jet-driven emission-line kinematics (e.g., Cecil 1988; Axon et al. 1998; Veilleux & Bland-Hawthorn 1997; Veilleux et al. 1999; Ferruit et al. 1999; Capetti et al. 1999; Cooke et al. 2000; Cecil et al. 2000, 2002). Closely related studies of radio galaxy emission-line regions have also shown both morphological and kinematic evidence for jet-gas interactions (e.g., Heckman et al. 1982; Baum, Heckman, & van Breugel 1992; Gelderman & Whittle 1994; Clark et al. 1998; De Vries et al. 1999; Axon et al. 2000; Tadhunter et al. 2000; Best, Röttgering, & Longair 2000). Brief reviews of the field can be found in the recent UNAM conference Emission Lines from Jet Flows (see articles by Capetti 2002; Ferruit 2002; Veilleux et al. 2002; Best et al. 2002; and Tadhunter 2002).

Despite the progress resulting from these studies, there are a number of outstanding questions. (1) What determines whether the radio- and line-emitting phases remain separate or interpenetrate? Previous work has yielded good examples of both situations. (2) What are the differences between "lobe" and "jet" environments? There is some evidence for a different radio/emission-line dependency in these two cases (e.g., Capetti et al. 1996). (3) What types of velocity field result from the interaction? With relatively few detailed kinematic studies, little is known beyond the general identification of bipolar flows (blue-/redshifted components straddling the nucleus), possible lateral expansion and/or conical expansion (line splitting), and generally enhanced turbulence (large line widths). (4) What are the acceleration mechanisms of the ionized gas? Possibilities include cloud acceleration by shocks, sweeping, cloud ablation, entrainment, or coherent ram pressure. (5) What are the roles of shocks? Do they simply act to compress and sweep gas, or do they play a more significant role in ionizing the gas as argued, for example, by Dopita & Sutherland (1995, 1996)? Stated slightly differently: (6) What determines the relative importance of the nuclear far-UV radiation field and the influence of the radio jet in ionizing and heating the gas? (7) What is the effect of the interaction on the radio flow? Under different circumstances, a radio jet/flow might be disrupted, deflected, entrain material or pass clouds unaffected. (8) Conversely, what is the effect of the interaction on the line-emitting gas? Gas clouds might be unaffected, dispersed, ablated, accelerated coherently or accelerated while breaking up. (9) What is the evolution of the interaction? As the interaction proceeds, how do the radio and emission distributions change and on what timescale?

In the hope of answering some of these questions, we have chosen to study one of the best examples of jet-gas interaction in a Seyfert galaxy, Mrk 78. The unusual kinematic and morphological nature of the nuclear regions of this galaxy were first recognized by Sargent (1972) and Adams (1973), while the triple radio source was first mapped by Wilson & Willis (1980) and Ulvestad, Wilson, & Sramek (1981). In the long-slit survey by Whittle et al. (1988), Mrk 78 stood out as having an exceptionally prominant bipolar flow, with $\sim$50% of the NLR flux in two components with velocities of +680 and -480 km s^{-1} relative to systemic. Further work by Pedlar et al. (1989) confirmed the prominance of the bipolar flow and provided improved radio and [O III] images. Using *HST* Faint Object Camera (FOC) images, Capetti et al. (1996) argued on morphological grounds for the importance of the radio interaction with the emission region.

For the present study, we add a deep *HST* [O III] image, a sensitive 3.6 cm VLA radio map, an *HST* near-UV continuum image, and 10 Faint Object Spectrograph (FOS) spectra spanning the emission region. Together, we believe these allow a significantly richer analysis of the processes occurring in the NLR of Mrk 78.

In § 2, we introduce the various data sets and reduction methods, while in § 3 we describe the optical and radio images. In § 4, we assess possible signatures of the likely physical processes through a detailed comparison of the radio and [O III] images. After constructing a plausible physical description of the radio flow pattern and response of the line-emitting gas, we introduce in § 5 the kinematic data from the 10 FOS spectra. This allows a more confident description of the region, and in § 6 we distill the results into a number of distinct physical mechanisms that we feel have been identified. In companion papers, we make use of new Space Telescope Imaging Spectrograph (STIS) data to explore more fully the ionization and dynamical processes.

For basic reference (e.g., Whittle 1992a): Mrk 78 is an early type, possibly peculiar, galaxy, with $B_T = 15.24$ and $B_T^o = 15.02$. A heliocentric systemic redshift of $cz = 11052$ km s^{-1} gives a distance of 147 Mpc, a scale of 714 pc arcsec^{-1} and a luminosity of $M_B = -20.82$ for $H_0 = 75$ km s^{-1} Mpc^{-1}, which we use throughout.

2. OBSERVATIONS AND REDUCTION

A wide range of observations of Mrk 78 has been gathered for this study, including *HST* images in continuum and emission lines, multiaperture spectra, and VLA radio imaging. Tables 1 and 2 give basic information on the images and spectra, while Figure 1 shows all relevant optical filter curves superposed on a spectrum of Mrk 78. The PC data provide a high signal-to-noise ratio (S/N) [O III] λ5007 image, while the archival FOC images provide a check on the [O III] image, a rather low S/N [O II] λ3727 image, and continuum images at V and U. Our FOS spectra target 10 locations, all of which furnish [O III] kinematic information and half of which furnish full optical coverage. Our 8 hr VLA radio observation at 3.6 cm provides

TABLE 1
HST Image Data

Camera (1)	Data Set (2)	Date (3)	Filter (4)	Exp. (s) (5)	λ_{pk} (Å) (6)	$\Delta\lambda$ (Å) (7)	QT_{pk} (8)	Use (9)
PC.....	W1200101T	1992 Aug 29	F517N	1608	5170	88	0.120	[O III]-on
	W1200102T	1992 Aug 29	F517N	1800	5170	88	0.120	[O III]-on
	W1200103T	1992 Aug 29	F517N	1606	5170	88	0.120	[O III]-on
	W1200104T	1992 Aug 29	F588N	900	5880	43	0.117	[O III]-off
	W1200105T	1992 Aug 29	F588N	900	5880	43	0.117	[O III]-off
FOC.....	X0L30601T	1991 Sep 19	F502M	1665	4940	530	0.019	[O III]-on
	X0L30602T	1991 Sep 19	F550M	1796	5460	188	0.009	[O III]-off/*V* band
	X0L30603T	1991 Sep 19	F130M	931	1280	88	0.001	Far-UV
	X2580303T[a]	1994 Mar 19	F502M	800	4940	530	0.019	[O III]-on
	X2580304T[a]	1994 Mar 19	F550M	1195	5460	188	0.009	[O III]-off/*V* band
	X2580302T[a]	1994 Mar 19	F372M	896	3710	406	0.049	[O II]-on
	X2580801T[a]	1995 Mar 19	F342W	596	3410	702	0.055	[O II]-off/*U* band
	X2580301T[a]	1994 Mar 19	F320W	596	3360	844	0.060	Near-UV
	X2580305T[a]	1994 Mar 19	F210M	596	2150	214	0.004	Mid-UV

[a] Post-COSTAR.

a sensitive radio image with comparable resolution to *HST*. We briefly describe the observations and data reduction.

2.1. *HST PC Images*

Mrk 78 was observed using the pre-COSTAR Planetary Camera on *HST* for a total of 5014 s in F517N and 1800 s in F588N. The field of each chip is approximately $35'' \times 35''$ with pixel size $\sim 0''.04414 \times 0''.04414$. Figure 1 shows the exceptional match of the redshifted [O III] $\lambda\lambda$4959, 5007 lines to the narrow F517N filter (designed for zero-redshift Mg I *b*), which has a high and constant throughput across the full [O III] velocity range (see inset). The resulting image has high S/N and is dominated by the [O III] lines that make up $\sim$72% of the detected flux.

Reduction followed standard procedure. Bias subtraction and flat fielding were done in the pipeline, while cosmic-ray removal and background subtraction were done using IRAF. These cleaned, combined images are shown in Figures 2*a* and 2*b*. We smoothed the continuum image using a nested sequence of Gaussians (FWHM = 0".2 for $R < 2''$, FWHM = 0".4 for $2'' < R < 4''$, and FWHM = 1".0 for $R > 4''$), effectively preserving near-nuclear structure while reducing noise on larger scales. This smoothing is important, since the scaling factor required to match the F517N continuum contamination is quite large (6.37, from the filter transmissions and continuum slope). The smoothed continuum and continuum-subtracted on-band images are shown in Figures 2*c* and 2*d*. We used the Lucy (1974) routine in STSDAS to deconvolve this last continuum-subtracted [O III] image. Note that deconvolution after continuum subtraction is legitimate in this case because the point-spread functions (PSFs) for the F517N and F588N filters are so similar. The deconvolution converged after 120 iterations, and this image is shown in Figure 2*e* together with the TIM PSF in Figure 2*f* (similar results were obtained using the PSF from an image of a nearby SAO star).

Conversion factors to flux were evaluated using the appropriate photometric parameters and filter curves. Our measured

TABLE 2
HST FOS Data[a]

Ap No. (1)	Intended Target (2)	$\Delta\alpha$[b] (arcsec) (3)	$\Delta\delta$[b] (arcsec) (4)	Exposure (s) G400H (blue) (5)	G570H (green) (6)	G780H (red) (7)
1.....	LW-1	0.00	0.00	720	720	910
2.....	LW-2	−0.71	−0.37	...	900	...
3.....	LW-4	−1.42	−0.02	1570	900	1770
4.....	LW-5	−2.25	+0.03	1560	900	1860
5.....	LW-3	−1.30	+0.63	...	900	...
6.....	LW-gap	−0.72	+0.33	2280	1440	2280
7.....	Nucleus	+0.38	+0.19	...	1440	...
8.....	LE-1	+1.08	+0.39	750	720	720
9.....	LE-iNfan	+1.47	+0.75	...	840	...
10.....	LE-iSfan	+1.73	+0.31	...	840	...

[a] Program GO 5471, on 1995 March 26, from files Y2BA0101T–Y2BA010TT.
[b] From Ap 1.

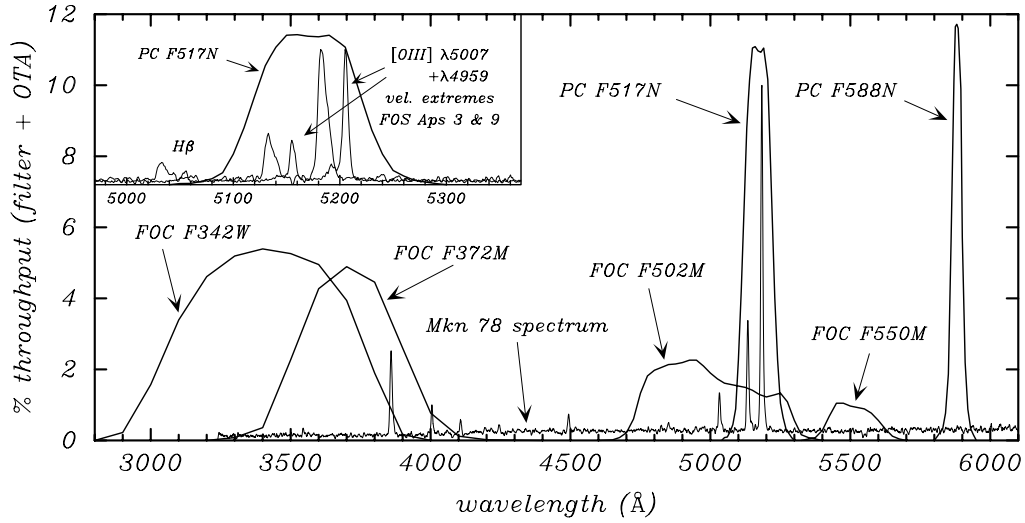

FIG. 1.—*HST* filter curves showing total throughput (filter + telescope + detector) superposed on a spectrum of Mrk 78 (FOS aperture 6). Note the exceptional match of the PC F517N filter to the [O III] lines. The inset plot confirms that the F517N throughput is essentially constant across the entire NLR velocity range ([O III] $\lambda\lambda$4959,5007 lines from FOC Ap 3, -600 km s^{-1} and Ap 9, +700 km s^{-1}, are shown).

total continuum and [O III] fluxes agree well with the ground based 10″ multichannel spectrophotometer data of de Bruyn & Sargent (1978; $F_{\lambda,5880} = 3.63$ vs. 3.20×10^{-15} ergs s^{-1} cm^{-2} Å^{-1} and $F_{5007} = 6.53$ vs. 6.38×10^{-13} ergs s^{-1} cm^{-2}; the first value in each pair is ours).

2.2. *HST FOC Data*

Several images of Mrk 78 have been taken using the FOC, both pre- and post-COSTAR (see Table 1). Since most of these data have been presented elsewhere (Capetti et al. 1994, 1996), we give here only a brief description. The pre-COSTAR images were kindly made available by Capetti, while the post-COSTAR images were taken from the archive and reduced following the approach described above for the PC images, including the use of a nested smoothed continuum image for off-band subtraction. Figure 3 shows a montage of the various post-COSTAR FOC images, together with our PC [O III] and VLA radio images (all are plotted to the same spatial scale, with logarithmic gray scales labeled in flux units).

Consider first the two [O III] images. The PC image has far higher S/N (∼55 times in terms of detected [O III] signal and one-third the on-band continuum contamination), but the FOC image is unaberrated and has intrinsically higher resolution. A comparison is therefore useful and shows gratifying similarity. Not only are all the major [O III] features visible in both, but many of the weaker features seen in the PC image are also just discernible in the FOC image. Figure 4*a* shows our final deconvolved PC image as a contour plot, with securely identified features labelled (see § 3.4 for a more detailed discussion of these features).

The only area of significant difference between the PC and FOC [O III] images is the near-nuclear region where reddening complicates simple continuum subtraction. The FOC filter combination is much more vulnerable to this problem (the on-band image contains ∼72% continuum), and so large negative residuals occur over the nuclear region following continuum subtraction properly scaled to match the outer region (see Fig. 3*b* and the figures in Capetti et al. 1994, 1996; note that a black zero level in all their plots hides the extent of the problem).

Figure 3*e* shows the FOC F550M pure continuum image. Comparison with our PC F588N image shows good agreement, both in the nuclear regions and after smoothing at lower flux levels away from the nucleus. Although the FOC image contains only ∼30% of the signal detected in the PC image, it is nevertheless a superior image, with its zero readout noise and unaberrated PSF. It is our image of choice for studying the *V*-band continuum.

Figure 1 shows that the FOC F342W filter provides an almost pure *U*-band continuum, with a small emission-line contamination from [O II] λ3727, [Ne V] λ3425 and Mg II λ2800 (the latter is beyond the plotted FOS spectrum). Taking mean line flux ratios from the FOS data (and Mg II from Ferland & Osterbrock 1986), we use the F342W filter curve to estimate a total emission-line contamination in the F342W image of 6.6%, divided 3.7%, 2.8%, and 0.1% between the three lines, respectively. We use a scaled version of the PC [O III] image to remove this contamination, calling the resulting pure continuum image F342Wc ("c" for corrected), which is shown in Figure 3*f*. This is, in fact, visually indistinguishable from the original F342W image. The F342Wc image is remarkable both in its difference from the F550M *V*-band continuum and in its similarity to the [O III] image, as discussed further in § 3.2. We note that a further FOC image, F320W, shows very similar structure to the F342W image, but because of its poor centering in the FOC field we make no further use of it (neither of these UV images was included in the studies by Capetti et al.)

The F372M and F342Wc images constitute an [O II] λ3727 on- and off-band pair. While their proximity in wavelength ensures a color insensitive subtraction, the continuum contamination in F372M is high (∼76%), yielding an [O II] image of rather low S/N. This [O II] image is shown in Figure 3*d* and, at least superficially, resembles the [O II] image in Capetti et al. (1996), who used the F550M image for the off-band.

Finally, we have checked the total continuum and line fluxes in the FOC images against the ground-based measurements of de Bruyn & Sargent (1978), finding excellent agreement.

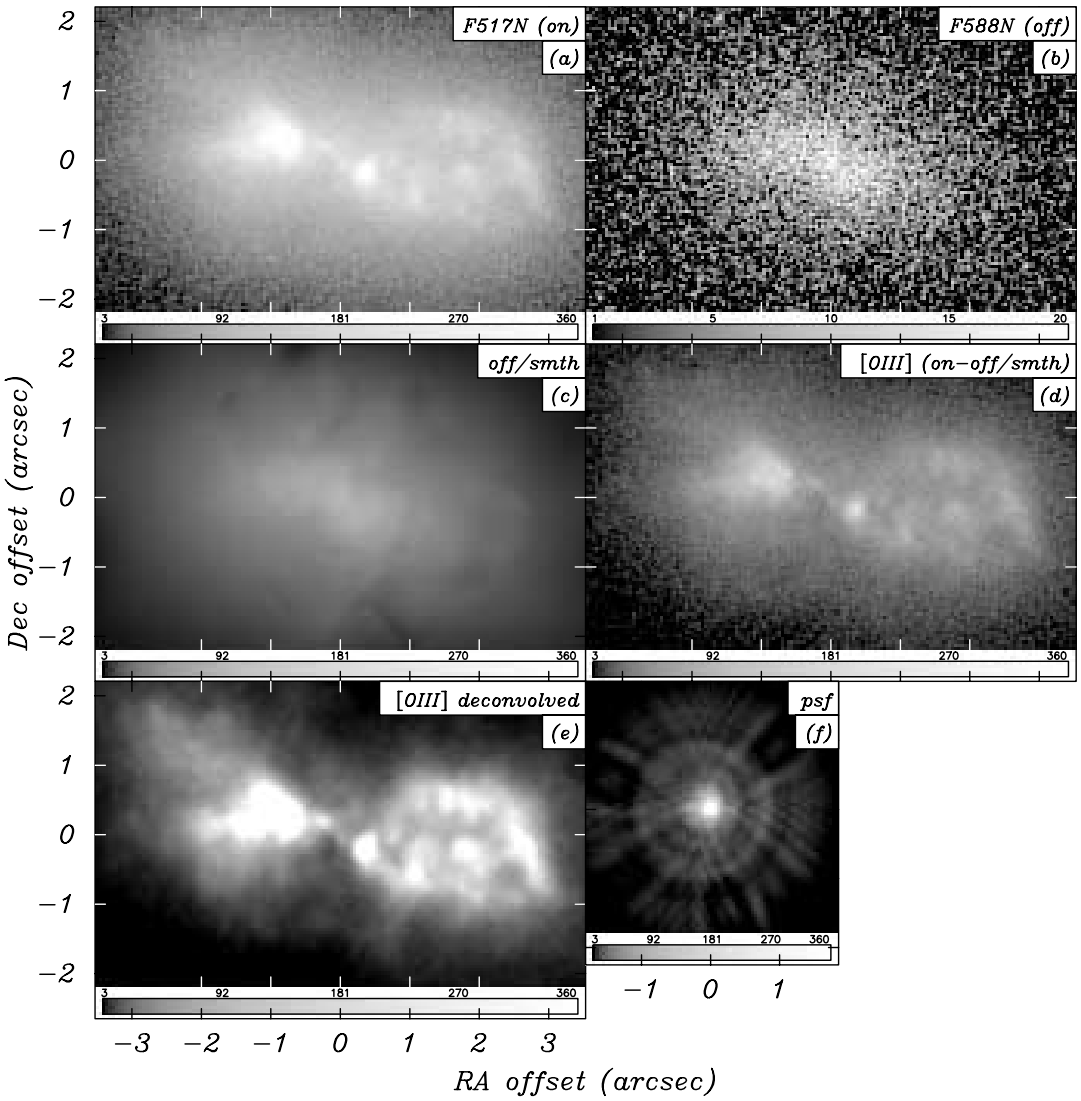

FIG. 2.—Stages in preparing the [O III] image from PC data on Mrk 78. Below each image is shown the (logarithmic) response function (*gray scale*) labeled in DN per pixel (where 1 DN = 7.5 e^-). (*a*) F517N on-band image (line plus continuum). (*b*) F588N off-band image (pure continuum). (*c*) Same as (*b*), after nested Gaussian smooth and multiplicative scaling to match the on-band image. Noise is greatly reduced while resolution near the center is approximately preserved. Note how little the continuum contaminates the on-band image (~28%; both are shown with the same response function). (*d*) [O III] line image resulting from the subtraction of (*c*) from (*a*). (*e*) [O III] line image following Lucy deconvolution using the PSF shown in (*f*). Except for (*b*), all images are shown with the same response function.

2.3. *VLA* 3.6 cm *Images*

The VLA was used in A array to observe Mrk 78 for a total integration time of 8 hr at 3.6 cm. Flux calibration sources were 1328+307 and 0134+329, and reduction followed standard procedure within AIPS. Two maps were generated; one using uniform-weight yielding a beam of $0\farcs16 \times 0\farcs15$ in P.A. $= 10^\circ$ with a noise level of 16 μJy beam^{-1}, and the second using natural-weight and yielding a beam of $0\farcs29 \times 0\farcs27$ in P.A. $= 12^\circ$ with a noise level of 9 μJy beam^{-1}. No polarized flux was detected.

Figures 3*c* and 4*b* show the higher sensitivity but lower resolution data, while Figure 5 and the center of Figure 3*c* show the higher resolution core data. To see the extended core structure more clearly, Figure 5*b* shows the data after a point source of 3.8 mJy has been subtracted. The location and strength of this source were carefully chosen to yield the least "pathological" residual—no negative flux, no peculiar near-nuclear morphology. An alternative approach is shown in Figure 5*c*, which uses Lucy deconvolution to yield a super-resolved image, although some artifacts may be introduced on the eastern side where the jet flux is much weaker. Salient features are labelled in Figures 4*b* and 5*b* and are discussed further in § 3.5.

2.4. *HST FOS Spectra*

To study both kinematic and ionization conditions within the nebulosity, we obtained FOS spectra at 10 locations using the $0\farcs43$ circular aperture. Table 2 gives the features targeted, their relative positions, and the exposures obtained. Our intention was to take spectra at all 10 locations using G570H to map the velocity field using the [O III] λ5007 profile and take UV and optical spectra using G190H, G400H, and G780H at five of these locations (LW-1, -4, and -5, LE-1a, and LW-gap; see Fig. 4*a* for feature identification) to study the ionization conditions. Regrettably, the *HST* target acquisition was less than perfect. Although our PC image gave an accurate offset from a nearby $V \sim 13.2$ mag star to knot LW-1 ($41\farcs29$ in P.A. $125\fdg84$, J2000.0), the actual executed offset was different

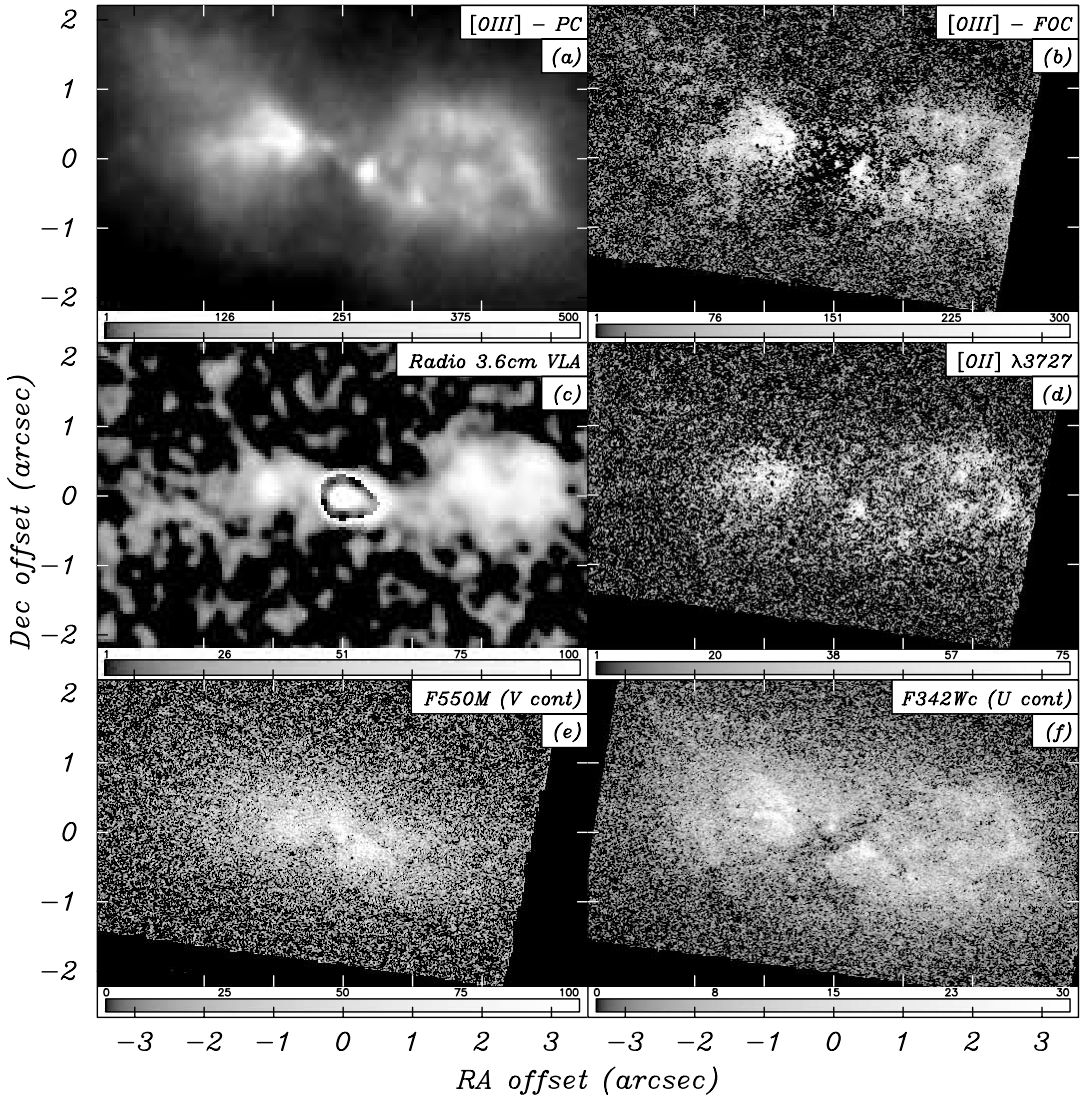

FIG. 3.—Emission-line, radio, and continuum images of Mrk 78. (*a*) Deconvolved [O III] PC image, as shown in Fig. 2*e*. (*b*) Post-COSTAR FOC [O III] image constructed from F502M (on, not shown) and F550M (off) images. (*c*) VLA 3.6 cm natural-weight radio image. To show the core more clearly, a scaled ($\times 0.2$) uniform-weight image has been substituted above 200 μJy beam^{-1}. (*d*) [O II] λ3727 image, constructed from the FOC F372M (on, not shown) and F342Wc (off) images. (*e*) FOC F550M pure continuum image (approximately *V*-band). (*f*) FOC F342Wc pure continuum image (approximately *U*-band), constructed from the F342W image with small ($\sim$6%) correction for [O II] λ3727, [Ne V] λ3426, and Mg II λ2800 line contamination (the F342W and F342Wc images are visually indistinguishable). All response functions are logarithmic. Surface brightness units are times 10^{-15} ergs s^{-1} cm^{-2} arcsec^{-2} for line images (*a*, *b*, *d*), times 10^{-17} ergs s^{-1} cm^{-2} Å^{-1} arcsec^{-2} for continuum images (*e*, *f*), and μJy beam^{-1} for the radio image (*c*).

and placed all apertures at an additional offset of 0.″66 in P.A. 217°.[2] Establishing the actual aperture locations was achieved in several ways. First, we assumed that the *relative* aperture placement was correct, since these smaller offsets within the emission-line region were all executed following the single main acquisition offset. Second, we compared an undispersed observation taken through the 4.″3 FOS acquisition aperture with PC and FOC images. Third, we measured [O III] λ5007 line and continuum fluxes from the FOS spectra and found the best-fit (minimum χ^2) match to artificial apertures that sampled both PC and FOC line and continuum images. All these methods gave consistent results and suggest the apertures were, in fact, located as shown in the central part of Figure 6, with an uncertainty of roughly $\pm$0.″15. Unfortunately, as can be seen from Figure 6, with a couple of exceptions, most of the emission-line knots were missed.

All spectra were reduced and calibrated within the CALFOS pipeline, and data from the same aperture combined to give a single spectrum. Figure 6 shows the spectra from all ten apertures. Measurement and analysis of the emission-line strengths is presented in a companion paper, while the [O III] profiles and associated velocity field are discussed in § 5.

3. DESCRIPTON OF IMAGES

In describing the various images, we identify features using "L" (line), "R" (radio), "C" (continuum), "E" (east), and "W" (west), followed by other descriptive or numerical qualifiers. As described in detail in § 3.7, we adopt an optical coordinate frame based on the astrometry of Clements (1981), with origin close to the southern nuclear component (which we refer to as CNuc-S; see § 3.1) visible in the FOC F550M image (0, 0 in all optical figures corresponds to

[2] A different offset resulted for the UV observations. We are confident of the accuracy of our requested offset and suspect that tracking was lost during the relatively large slew.

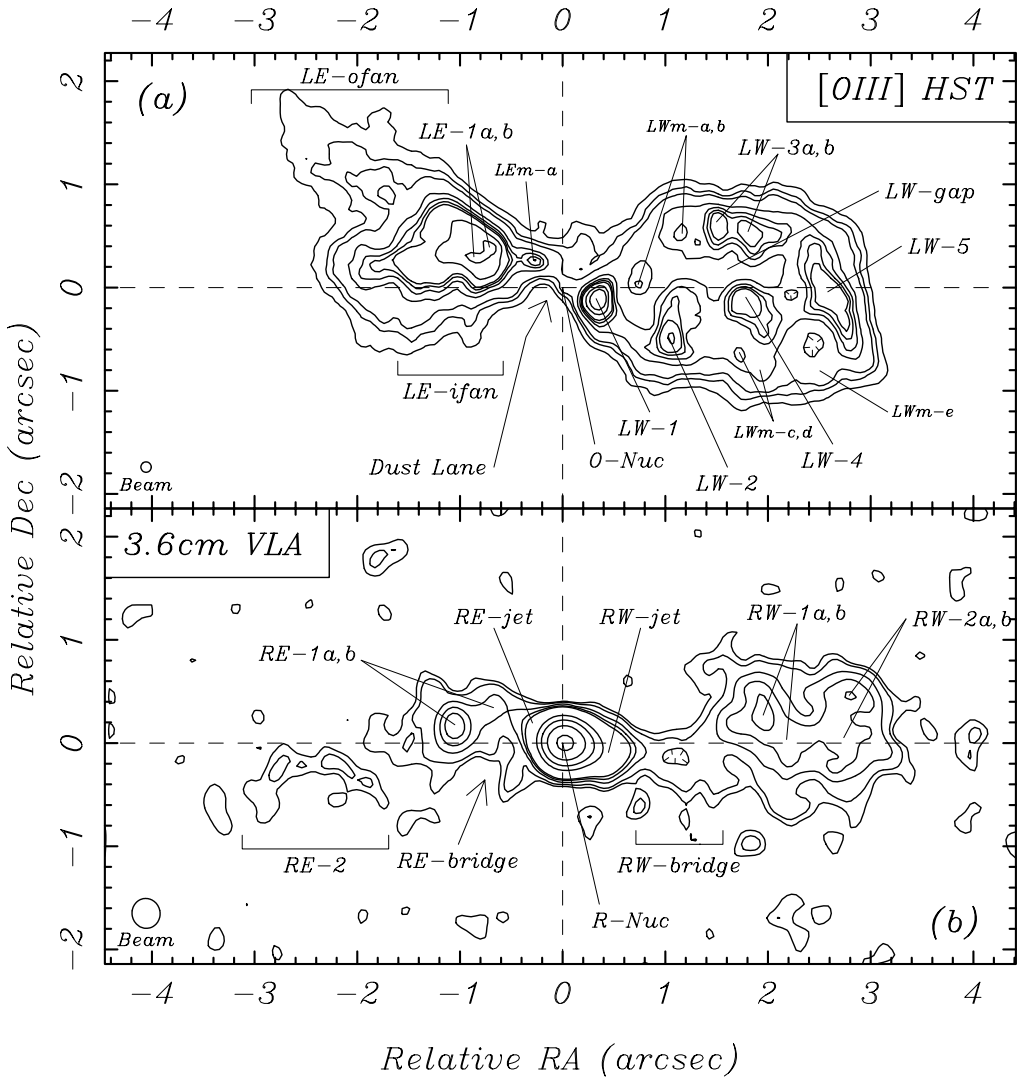

FIG. 4.—Mrk 78 feature identification. (*a*) [O III] image with contour levels at 10, 15, 20, 40, 60, 80, 100, 200, 400 × (1.20 × 10^{-15}) ergs s^{-1} cm^{-2} $arcsec^{-2}$. Major and minor features are labeled. (*b*) 3.6 cm VLA natural-weight image (beam 0.″29 × 0.″27 in P.A. 12°). Contour levels are at 15, 25, 50, 75, 100, 500, 1000, 2000, 4000 μJy $beam^{-1}$. Major features are labeled.

$7^h37^m56^s.828 \pm 0^s.016, +65°17'42''.24 \pm 0''.10$, B1950.0, FK4). We now describe the continuum, emission-line, and radio morphology of Mrk 78.

3.1. *V-Band Continuum Morphology*

On large scales, ground-based continuum images of Mrk 78 show a relatively smooth elliptical morphology with no obvious spiral structure (e.g., Adams 1973; DeRobertis 1987; Capetti et al. 1996). At radii $r \gtrsim 4''$, the surface brightness approximately follows an $r^{1/4}$ law, and the isophotes are well fitted by concentric aligned ellipses ($e = 1 - b/a = 0.45 \pm 0.02$; $a_3, b_3, a_4, b_4 \lesssim 0.02$, P.A. $= 81° \pm 1°$, ΔR.A.$_0$, Δdecl.$_0 \lesssim 0''.2$; note that, from RC3, the ellipticity is also 0.45 on the largest scales of $D_{25} = 25''$). Within $\sim 1''.5$, there is a marked increase in nonelliptical residuals (a_3, b_3, a_4, and b_4), and both PC and FOC images show a quasi-triple structure with a dust lane running across the center along P.A. $\sim 138° \pm 10°$ (see Figs. 2*b*, 2*c*, and 3*e*, of which Fig. 3*e* is the clearest). We refer to these continuum components as CE, CNuc, and CW, where CNuc has a double nature, CNuc-N and CNuc-S. Of these, CE and CW are clearly extended, while the CNuc-N,S components are more compact. As discussed in § 3.7, CNuc-S is within $\sim 0''.15$ of the radio core and is almost certainly the true (active) nucleus just visible through the dust lane. A recent NICMOS image at 1.6 μm is essentially featureless, confirming that all structure seen in the optical results from patchy obscuration and/or sources of blue light.

Several features suggest that Mrk 78 is in a postmerger state: an approximate $r^{1/4}$ law luminosity profile, complex nuclear structure including dust lanes, and a highly extended asymmetric gas distribution (see § 3.3 below). If this conjecture is true, the merger was not very recent, since on large scales the galaxy continuum is fairly smooth and symmetric. We note that from ground-based data DeRobertis (1987) also argued for a merger but for somewhat different reasons. He interpreted the double velocity profile and a slightly off-centered brightness peak as evidence for two kinematically distinct nuclei. From the current data, we are confident that the double velocity field arises from a jet-driven bipolar flow, and the complex nuclear appearance comes from patchy obscuration. Evidence for an approximately relaxed single system comes from the smooth NICMOS image, a normal stellar velocity dispersion (Nelson & Whittle 1995), and the fact that there is a single well-defined radio nucleus located behind the dust lane.

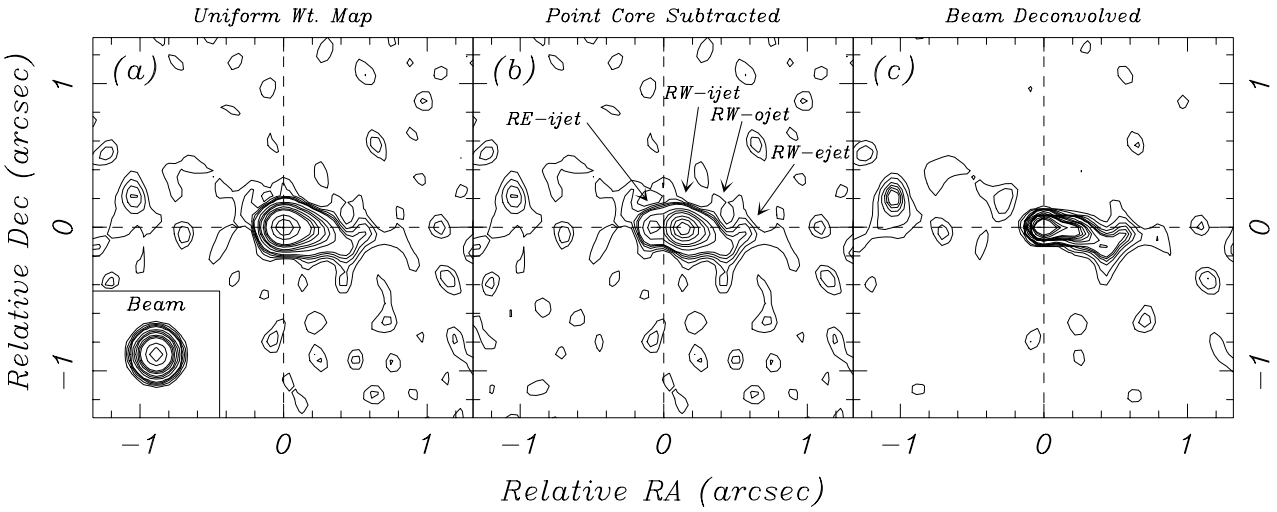

FIG. 5.—3.6 cm VLA uniform-weight data. Contour levels are 20, 40, 60, 80, 100, 200, 300, 400, 600, 800, 1000, 2000, 3000, 4000 μJy beam^{-1}. (*a*) Mrk 78 core region, with beam shown (0.″16 × 0.″15 in P.A. 10°). (*b*) same data with 3.8 mJy nuclear point source subtracted and inner components labeled. (*c*) Same data, deconvolved using beam shown in (*a*).

3.2. *U-Band Continuum and Color Distribution*

Figure 3*f* shows the pure *U*-band continuum, F342Wc. This is a remarkable image, both in its difference from the *V*-band continuum image and in its similarity to the [O III] line image. The main dust lane is clearly visible, with possible additional absorption features to the south and west. As expected, the nuclear components are significantly weaker than in the *V*-band image, although CNuc-N is still visible. The near-nuclear components, CW and CE, resemble the [O III] line image much more than in the *V*-band continuum image, with CE showing a double ridge fan structure and CW resembling the bright [O III] knot LW-1. At larger radii, both to the east and west, the *U*-band structure resembles the complex knots seen in [O III]. After suitable smoothing, Figure 7 shows the continuum ratio color image, $F_{\lambda,5500}/F_{\lambda,3420}$ (light is red, dark is blue), with [O III] contours overplotted. Nuclear reddening is clearly visible, as is the bluer color of the extended regions, particularly those underlying the [O III] knots of LE-1, LE-ifan, LW-3, LW-4, and possibly LW-5. Flux ratios range from $\sim$10 across the nucleus to $\sim$1 or less in the bluest regions. These values are broadly confirmed by our FOS spectra, although unfortunately none of our apertures fall on blue knots, with the exception of Ap 4, which falls on the tip of LW-5 (off the color image) with a flux ratio of $\sim$0.8. For reference, a typical unreddened S0 galaxy has a flux ratio $F_{\lambda,5500}/F_{\lambda,3420} \sim 2.5$–3.0 (Kennicutt 1992).

It seems that Mrk 78 is a clear example of an object with an "extended blue continuum." This component, seen in many active galactic nuclei (AGNs), has received considerable attention recently. Its origin is still unclear, although possibilities include nebular emission, scattered nuclear AGN light, emission from shocks, and recent star formation. In a companion paper, we consider the origin of this component in Mrk 78 in more detail.

3.3. *Extended Narrow-Line Region (ENLR)*

Figure 8 presents a larger scale version of our deconvolved PC [O III] image, revealing the low surface brightness ENLR emission. Some artifacts of deconvolution may affect the faint emission in this image, including small-scale structure (amplified noise) and the rather steep decline of flux to the north and south. Using the undeconvolved data, the surface brightness in the western ENLR is $\sim 4-6 \times 10^{-16}$ ergs s^{-1} cm^{-2} arcsec^{-2}, with a total flux of $\sim 3.8 \times 10^{-14}$ ergs s^{-1} cm^{-2} in a region 9″ × 13″ centered 10″ west and 1.″35 south of the nucleus. The overall form of the ENLR agrees very well with previous ground-based studies, showing the double extension to the west and southwest and a more truncated extension to the northeast (see, e.g., Adams 1973; DeRobertis 1987; Pedlar et al. 1989).

3.4. *NLR* [O III] *Morphology*

Figure 4*a* shows a contour plot of the inner [O III] line emission with features labeled. The emission region spans $\sim$6″ east-west and $\sim$3″ north-south, with a number of emission knots to the west and a more complex fanlike structure to the east. Across the nuclear regions running approximately south-southeast to north-northwest is a dark zone caused by the nuclear dust lane visible in the continuum images. Since this region is sensitive to continuum subtraction, its detailed [O III] structure is somewhat uncertain (see § 2.2), although there does seem to be a minor feature $\sim$0.″4 northeast of the nuclear (origin) position (LEm-a, where "m" means minor). Immediately outside the dust lane are the brightest emission-line features, LW-1 and LE-1.

Knot LW-1 is compact but slightly resolved. In the PC image, it appears to have an asymmetric brightness profile with the steeper side toward the nucleus. In the higher resolution FOC image, the eastern edge (toward the nucleus) is straight and approximately aligned with the edge of the dust lane. Thus, the knot shape and location may partly result from obscuration effects, with additional emission hidden behind the dust lane. As discussed below, however, the knot is located at the end of the radio jet, and so its shape and location may also be related to an interaction with the jet. The bright compact nature of the LW-1 knot makes it a possible astrometric reference point, particularly since the nuclear regions are so confused by dust. It is located 0.″34 west and 0.″13 south of our coordinate origin (see § 3.7).

The rest of the western region contains four additional major emission knots, each moderately well resolved (LW-2, -3, -4,

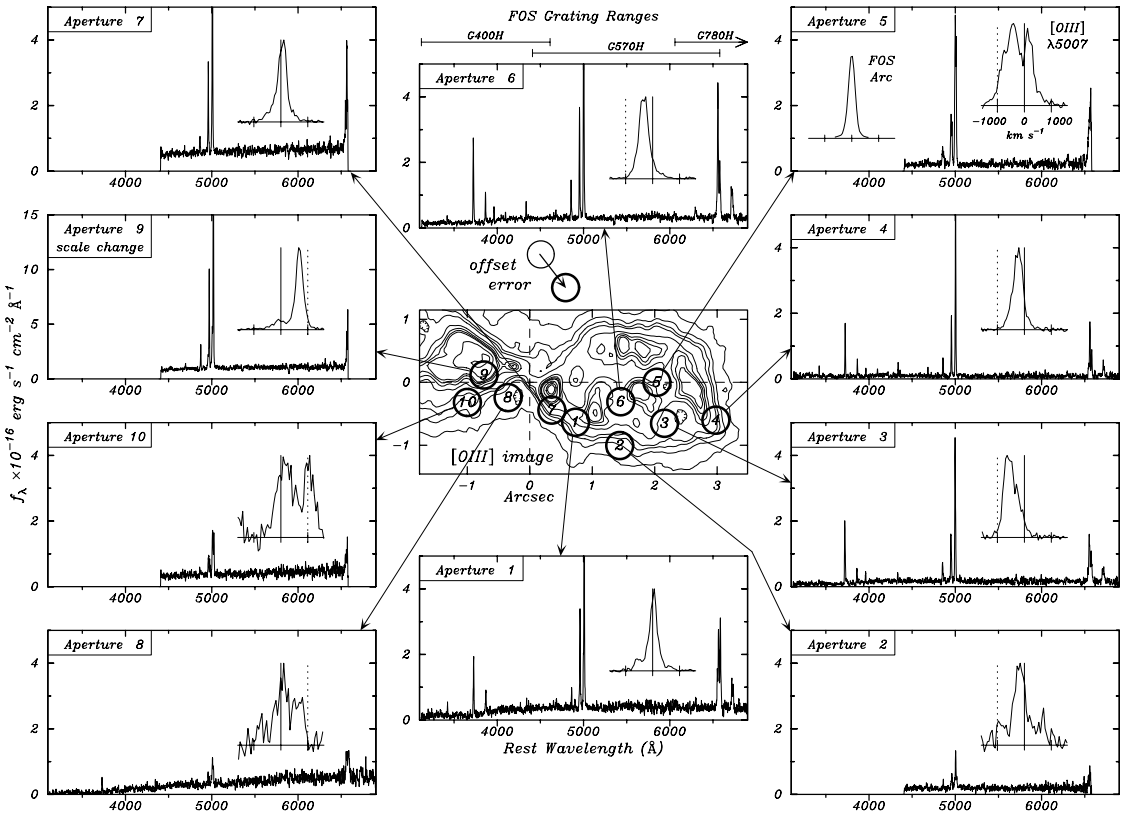

FIG. 6.—FOS optical spectra of Mrk 78. Central plot shows the [O III] PC image with true locations of the 10 FOS apertures (offset by 0.″66 in P.A. 217° from their intended position). Surrounding plots show FOS spectra shifted to zero redshift and smoothed by a box of width 5 Å. A blow up of the [O III] λ5007 profile for each spectrum is also given, with a key shown in Ap 5, including the FOS instrument profile. Combined spectra are shown for apertures with three grating observations (grating ranges are indicated at the top of the plot). Fluxes are in units of 10^{-16} ergs s^{-1} cm^{-2} Å^{-1}. All plots have the same peak height except Ap 9, which is different by a factor 3. In some plots, the [O III] λ5007 line is off scale, in which case the λ4959 line indicates the [O III] strength.

and -5), as well as a number of minor features that appear as weak peaks above a more general interknot background (LWm-a, -b, -c, -d, -e; "m" is minor). This interknot emission has a brightness of $\sim 3.5-5 \times 10^{-14}$ ergs s^{-1} cm^{-2} arcsec^{-2}.

Emission to the east forms a complex fanlike structure. The brightest region forms a compact double knot (LE-1a and -1b) that is located at the western end of a double ridge running eastward and northeastward from the nucleus to constitute a bright fan-shaped region (LE-ifan, where "ifan" = inner fan). At a significantly lower brightness level, this inner fan extends further east and northeast and separates into two ridges (LE-ofan, where "ofan" = outer fan). The southern boundary of this inner and outer fan appears corrugated, with about two "wavelengths" spanning $\sim$1.″5.

In Table 3, we present the [O III] λ5007 fluxes and average surface brightnesses for all the features labelled in Figure 4*a* using elliptical apertures (center, both axis diameters, and postion angle given in cols. [2]–[6]).

3.5. 3.6 cm *Radio Morphology*

Figure 4*b* shows the natural-weight radio map at the same scale as the [O III] image described above, with a number of features labelled. In addition to a strong central source, the emission is extended along P.A. $\sim$90°. A well resolved and quite complex "lobe" extends $\sim$1.″4–3.″0 west of the radio nucleus, with a rather abrupt edge at $\sim$3.″2. The lobe contains at least two main components each of which may be divided further (RW-1a and -1b, RW-2a and -2b). To the east is a low surface brightness feature extending $\sim$1.″8–3.″5 from the radio nucleus (RE-2). Between RE-2 and the nucleus is a brighter region comprising two components (RE-1a and -1b), one somewhat brighter than the other. These outer east and west lobes are connected to the core by weaker emission features that we loosely call "bridges" (RW-bridge and RE-bridge).

The nuclear region itself has interesting structure, which is seen most clearly using the higher resolution uniformly weighted data. Figure 5*a* shows this data for the core region, while Figures 5*b* and 5*c* show the data following point-source subtraction and Lucy deconvolution, respectively (see § 2.3). The core emission is certainly resolved, with flux to the west making up a bright inner extension at P.A. $\sim$270° (RW-ijet, where "ijet" means inner jet), becoming weaker and bending around to P.A. $\sim$237° (RW-ojet, where "ojet" means outer jet). This curved feature terminates abruptly at $\sim$0.″46 from the nucleus at P.A. 255° and spreads out approximately perpendicularly along P.A. $\sim$322° (RW-ejet, where "ejet" means end of jet). The situation to the east is less certain, but there also seems to be some residual flux after point-source subtraction immediately to the east (RE-ijet), with much weaker flux extending along P.A. $\sim$68°, which is the inner part of the RE-bridge feature. Thus, on the smallest scales ($\sim$0.″1 – 0.″2) a jet appears to emerge along P.A. $\sim$90° and 270°, stronger to the west, while on slightly larger scales the jet bends round to P.A. $\sim$70° and 240°, again stronger to the west.

Table 4 gives measured and derived properties for many of the radio features described above. Radio flux, mean surface brightness, and power (cols. [7], [8], and [9]) are

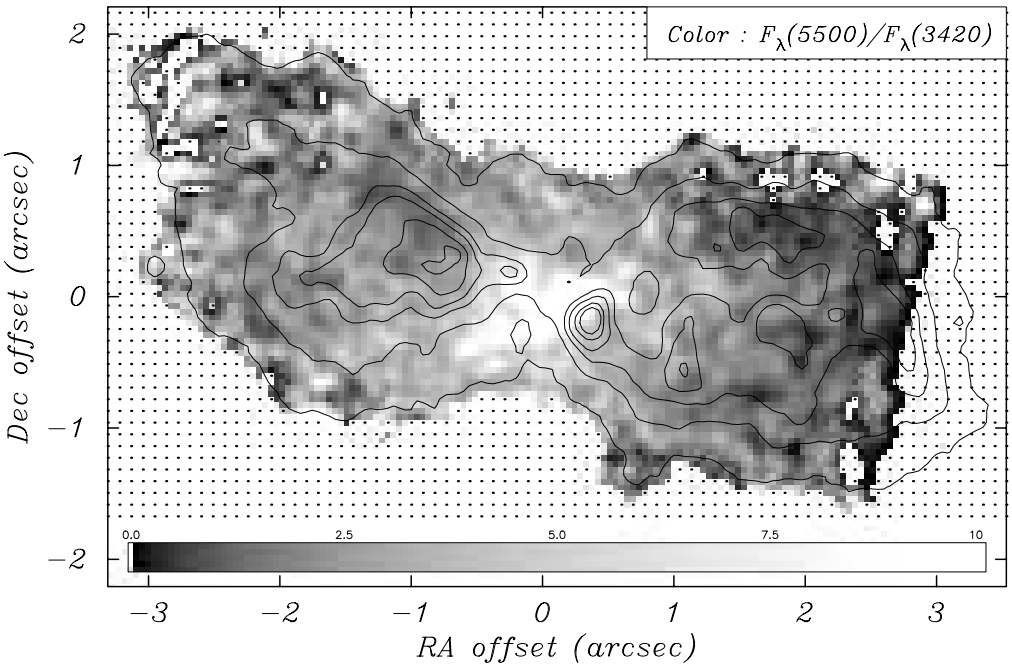

FIG. 7.—Gray-scale map showing the color distribution in Mrk 78, defined as the ratio of smoothed flux-calibrated FOC images F550M and F342Wc (see scale bar for ratio values). Superposed contours are from the PC [O III] image. Note the reddened nuclear region, as well as blue off-nuclear regions, particularly those near some of the [O III] knots. Regions of low S/N have been omitted. The truncated western side results from the edge of the FOC F550M image.

measured within elliptical apertures, whose center, axis diameters, and postion angle are given in columns (2)–(6). Also given are estimates of the magnetic field strength, pressure, and total energy (cols. [10], [11], and [12]). These estimates follow the formulation given in Miley (1980) and assume minimum energy conditions, spectral index $\alpha = -0.88$ between $\nu = 0.01$ to 100 GHz, and the filling factor, sine of the pitch angle, and ratio of energy in heavy particles to electrons all equal to unity.

3.6. *Comparison with Earlier Radio Data*

Previous VLA radio maps of Mrk 78 have been given by Wilson & Willis (1980), Ulvestad, Wilson, & Sramek (1981), and Pedlar et al. (1989). Of these, the study by Pedlar et al. is the most extensive, including integrations at 2 cm (2 hr), 6 cm (2 hr), and 18 cm (10 minutes). Here we give a brief comparison, since our more sensitive observations (8 hr at 3.6 cm), while agreeing in overall structure, do differ somewhat in detail. First, the integrated fluxes for the east, west, and central components all suggest an approximately constant spectral index ($\alpha \sim 0.88$, with $S \propto \nu^{-\alpha}$), and do not indicate any free-free absorption affecting the lower frequency emission. Second, the inner western jet, RW-ijet, is also seen in the 2 cm data of Pedlar et al., with a possible bend at 0.″2 to the west-southwest (see their Fig. 7*b*, beam 0.″15), although the fainter RW-ojet, RW-ejet, and RE-ijet are below the sensitivity limit of their 2 cm map. Third, although their natural-weight 6 cm map (their Fig. 7*d*, beam 0.″5) shows the same basic components that we find, the structures within these components do not correspond in detail. For example, the location and number of knots in the RW-lobe is different; their RW-bridge passes to the north, while ours passes to the south; their RW-jet is much less strong; and finally our RE-1 is a separate component, while it is an extension of the core in their map. These differences become more pronounced in their 6 cm uniform-weight map (their Fig. 7*c*, beam 0.″3) in which the extended features break up into discrete knots of similar intensity—three within RW-lobe and two within RE-1. Comparing with our 3.6 cm natural-weight map (Fig. 4*b*, beam 0.″28) again shows no correspondence in detail, with the possible exception of RE-1a. The reason for these differences is not entirely clear. One possibility is that the lobe surface brightnesses are sufficiently close to the noise limit in the Pedlar et al. 6 cm data that, although the lobes are reliably detected, their structure is not. Furthermore, the weakness of the RW-jet feature and the highly blobby nature of their uniform-weight 6 cm map suggest it may have been over-resolved when cleaned.

3.7. *Registration of Optical and Radio Images*

The all important alignment of the radio and optical images is somewhat uncertain, first because the *HST* reference frame is only accurate to $\pm 1''$, and second because there is no prominent optical nucleus to align with the radio core. We must therefore resort to using ground-based absolute astrometry to tie the optical and radio frames together. Clements (1981) gives the location of the blue-green continuum peak (IIa-O emulsion) to be $7^h37^m56^s.828 \pm 0^s.016, +65^\circ 17' 42''.24 \pm 0''.10$ (B1950.0, FK4). We assign this coordinate to the peak of the *HST* continuum images after smoothing by a Gaussian of FWHM = 1.″0 to simulate ground-based resolution. The location of the smoothed peaks coincide within $\pm 0''.05$ in the PC F588N and FOC F550M images and is, in fact, within 0.″05 of the southern nuclear component CNuc-S seen in the FOC F550M image. This location defines the coordinate origin in all our optical figures. It is located $0''.336 \pm 0''.05$ east and $0''.131 \pm 0''.05$ north of the compact [O III] knot LW-1.

Our 3.6 cm VLA core position is $7^h37^m56^s.847 \pm 0^s.016$, $+65^\circ 17' 42''.20 \pm 0''.10$ (B1950.0), which agrees well with

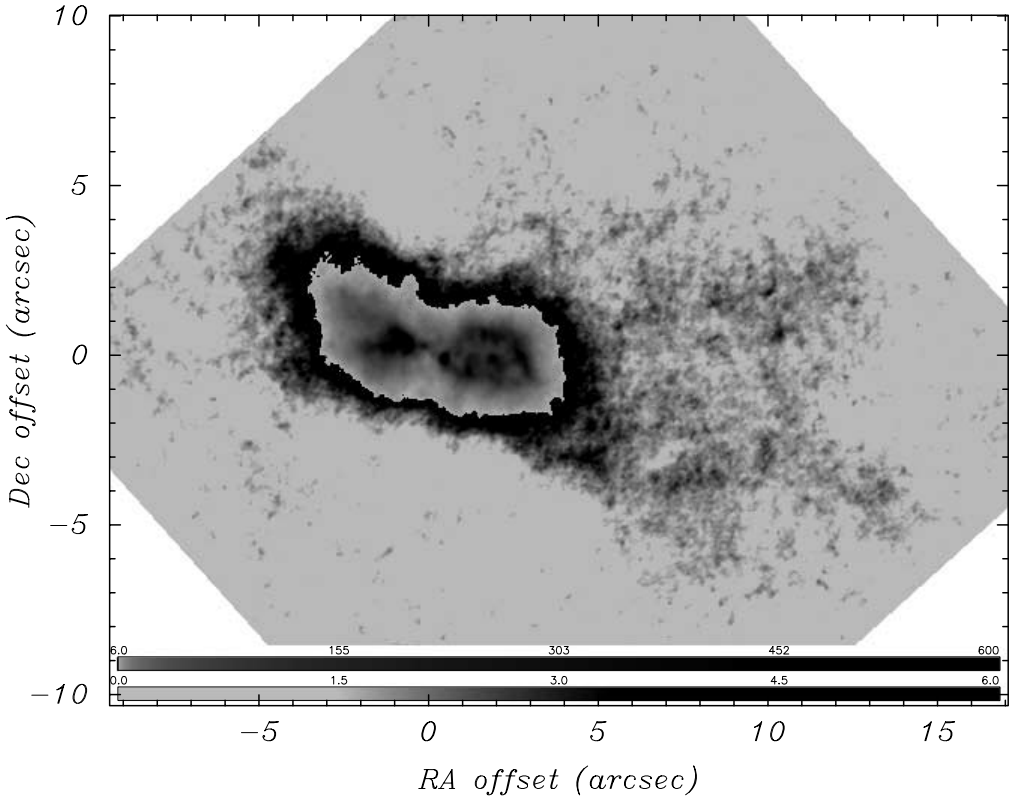

FIG. 8.—Large-scale ENLR in Mrk 78. Same as Fig. 2*e*, but including the full (rotated) PC6 chip, with double logarithmic response function showing both fainter outer emission and brighter inner emission. Response function bars are labeled in DN, where 1 DN = 7.5 $e^- = 7.77 \times 10^{-19}$ ergs s^{-1} cm^{-2} pixel^{-1} = 4.00×10^{-16} ergs s^{-1} cm^{-2} arcsec^{-2}. (The small-scale structure in the ENLR is not real and results from noise amplified by deconvolution).

previous VLA data (Ulvestad et al. 1981 6 cm, core offset $0\farcs08 \pm 0\farcs24$ east, $0\farcs25 \pm 0\farcs24$ north; Pedlar et al. 1989 2 cm, core offset $0\farcs02 \pm 0\farcs14$ east, $0\farcs01 \pm 0\farcs14$ north). The radio core position is therefore $0\farcs12 \pm 0\farcs14$ east and $0\farcs04 \pm 0\farcs14$ south from the smoothed optical continuum peak, which represents coincidence to within the errors. Figure 9 shows our 3.6 cm radio maps (*white contours*) plotted on top of our PC [O III] line map (*black contours*), using the above registration. There is circumstantial evidence that this is close to the correct placement. First, RW-jet coincides with the bright [O III] knot at LW-1 (Fig. 9*b*). Second, elliptical isophote fits to the continuum data *outside* the dust lane ($a = 1\farcs0-2\farcs5$) give a central location within $\sim 0\farcs15$ of both the radio nucleus and the smoothed continuum peak. Third, the radio position approximately matches the position of the CNuc-S feature, which is almost certainly the heavily reddened nucleus visible through the dust lane.[3]

Our radio location differs significantly from the one chosen by Capetti et al. (1996), who placed the radio core $0\farcs88$ east and $0\farcs23$ north from knot LW-1, arguing that this gave the best match between radio and [O III] structure in the lobes. However, this choice introduces three problems. First, their location is $0\farcs42$ east and $0\farcs14$ north from the optimum position demanded by astrometry—significantly greater than the $\pm 0\farcs10$ estimated errors. Second, the highly suggestive coincidence between [O III] knot LW-1 and RW-jet is lost. Finally, their placement of the radio core (and hence, presumably, the true nucleus) is just *outside* the central dust lane, raising the question of why the optical nucleus is not more visible. While we acknowledge some remaining uncertainty in the radio-optical registration, we feel the more central placement of the radio core behind the dust lane, as indicated by the astrometric data, is preferable.

We note, finally, our attempt to reduce the uncertainty in the *HST* reference frame. Several astrometric plates were taken using the 26 inch (0.7 m) Clark Refractor at McCormick Observatory to establish an accurate coordinate for the $V \sim 13$ mag star visible in our PC image (Mullis 1994). Unfortunately, we were unable to improve on the $\sim 0\farcs1$ accuracy of the Clements (1981) position for Mrk 78.

4. RELATION BETWEEN RADIO AND [O III] MORPHOLOGY

Figure 9 shows the *HST* [O III] image (*black contours*) superposed on the VLA 3.6 cm radio image (*white contours*; *top*: natural weight; *bottom*: uniform weight; coordinate registration taken from § 3.7, accuracy roughly $\pm 0\farcs1$). In this section, we use radio and [O III] morphology to help establish the global flow patterns of radio plasma and [O III] gas. We consider first the overall geometry, and then the western and eastern structures, starting at the nucleus and working out.

4.1. *Overall Geometry*

Before considering kinematics, we begin by asking to what extent the geometry of the emission-line region depends on hydrodynamic interaction with the radio source and to what

[3] Subsequent STIS and NICMOS images confirm that CNuc-S is indeed the hidden nucleus.

extent it depends on photoionization from a central source. For standard nuclear photoionization, one expects the emission to follow a biconical pattern whose axis is aligned with the innermost collimation axis.

In Mrk 78, this nuclear axis is somewhat ambiguous, partly because the optical nucleus is hidden by dust and partly because the radio source has two axes close to the nucleus: P.A. $\simeq 90^\circ$–270° on scales $\lesssim 0\farcs2$ and P.A. $\simeq 70^\circ$–240° on scales $\sim 0\farcs2$–$0\farcs6$ (more clearly defined on the west). If we associate the innermost axis with ionizing and radio collimation, then phenomena related to nuclear photoionization should have an axis of $\sim 90^\circ$–270°, while phenomena related to jet interaction should have an axis of $\sim 70^\circ$–240°, at least in the inner regions before the flow is further disrupted.

For the [O III] emission geometry, the inferred axes and opening angles *depend on the flux level*. At the brightest levels, the [O III] axis is defined by the innermost knots LE-1 and LW-1 located at P.A. $\sim 65^\circ$ and 255° (Fig. 4), with each knot showing a conical shape with apex on the side closest to the nucleus. Since these knots also coincide with the inner radio features RE-1b and RW-ojet (see below and Fig. 9), it seems likely that their geometry is at least partly determined by the jet-gas interaction.[4] At intermediate flux levels, the eastern *inner* fan (LE-ifan) has axis P.A. $\sim 72^\circ$, opening angle $\sim 34^\circ$, and apex $\lesssim 0\farcs2$ from the radio core. This feature may owe its shape to both jet-gas interaction and central source photoionization—its southern boundary is corrugated and cospatial with the deflected radio jet, while its northern boundary is straight and accurately aligned with both the nucleus and the outer fan ridge. At lower flux levels, the eastern *outer* fan (LE-ofan) has axis P.A. $\sim 84^\circ$, opening angle $\sim 58^\circ$, and apex $\lesssim 0\farcs15$ from the nucleus. Note also that its northern ridge is both far from any radio emission and kinematically quiescent (Pedlar et al. 1989). On the western side of the nucleus, the inner boundary of the [O III] lobe has axis P.A. $\sim 273^\circ$, opening angle $\sim 80^\circ$, and apex $\lesssim 0\farcs1$ from the nucleus. It would seem, therefore, that at these lower flux levels, central source photoionization plays an important role in defining both the morphology and boundary of the emission regions. Finally, at the lowest flux levels we find the same result. The western ENLR (i.e., the low surface brightness emission described in § 3.3) has approximately conical form, with axis P.A. $\sim 265^\circ$ and opening angle $\sim 50^\circ$ (Fig. 8). Since it lies well outside the radio source and has quiescent kinematics, it seems most likely to be ionized by the central source—a conclusion arrived at in a number of other studies (e.g., Unger et al. 1987; Pedlar et al. 1989). Note that the axis of the western ENLR is almost exactly 180° from the axis of the eastern outer fan (LE-ofan), lending support to the notion that these two features constitute a centrally illuminated bicone.

In summary, we find geometrical evidence for central source photoionization, particularly for the fainter and more extended regions. However, on smaller scales where the radio and [O III] emission regions overlap, there is evidence for direct hydrodynamic interaction. We now consider that evidence in more detail.

4.2. *Inner Western Compact Knot*

The western radio jet emerges due west and quickly bends west-southwest (Fig. 5), where it runs over the bright compact [O III] knot LW-1 (Fig. 9). Two things suggest an interaction in this region. First, right over LW-1, the radio jet first bends and then spreads out sideways, mainly to the northwest but also to the south. This seems to be a clear example of jet deflection and/or disruption with, in this case, a change in position angle first of $\sim 40^\circ$, then by $\sim 85^\circ$. Second, the LW-1 knot itself may show signs of the interaction. It has a "kidney bean" shape with limb brightening on the nuclear side and small wings pointing away from the jet, consistent with upstream jet compression and downstream expansion or ablation. In the highest resolution FOC image (Fig. 3*b*) the inner surface is flat, consistent with a cloud shock at this point. Although we have emphasized here a jet-related origin for the shape and location of LW-1, some ambiguity remains since the dust lane

[4] This is opposite to the conclusion of Capetti et al. (1994), who used the less sensitive radio map of Pedlar et al. (1989), which misses the position angle swing of the inner jet and its flaring over LW-1.

TABLE 3

[O III] λ5007 Feature Properties

	Elliptical Aperture								
Feature ID (1)	$\Delta\alpha_c$ (arcsec) (2)	$\Delta\delta_c$ (arcsec) (3)	a (arcsec) (4)	b (arcsec) (5)	P.A. (deg) (6)	Flux[a] (7)	SB[b] (8)	log Lum[c] (9)	log SL[d] (10)
L-total-(8.″8).....	0.00	0.00	8.80	8.80	...	65.3	1.1	42.23	34.75
LW-lobe-total	1.95	0.00	4.00	4.00	...	33.6	2.7	41.94	35.14
LE-lobe-total	−2.05	0.00	4.00	4.00	...	27.5	2.2	41.85	35.05
LW-1.....	0.34	−0.13	0.49	0.36	166	3.7	26.3	40.98	36.12
LW-2.....	1.08	−0.36	0.67	0.32	166	2.0	11.5	40.71	35.77
LW-3.....	1.72	0.52	0.85	0.39	71	2.8	10.3	40.86	35.72
LW-4.....	1.83	−0.22	0.63	0.41	51	2.3	11.1	40.77	35.75
LW-5.....	2.58	−0.09	1.04	0.42	26	3.7	10.7	40.98	35.74
LE-1	−0.89	0.36	0.60	0.44	65	7.8	37.7	41.30	36.28
LE-ifan	−1.08	0.33	1.17	0.95	69	16.5	18.8	41.63	35.98
LE-oNfan	−2.13	1.25	1.59	0.57	50	1.4	1.9	40.56	34.98
LE-oSfan	−2.09	0.16	0.89	0.62	99	1.7	3.8	40.64	35.28

[a] Units of 10^{-14} ergs s^{-1} cm^{-2}.
[b] Units of 10^{-14} ergs s^{-1} cm^{-2} arcsec^{-2}.
[c] Units of ergs s^{-1}.
[d] Units of ergs s^{-1} pc^{-2}.

TABLE 4
RADIO FEATURE PROPERTIES

Feature ID (1)	Elliptical Aperture $\Delta\alpha_c$ (arcsec) (2)	$\Delta\delta_c$ (arcsec) (3)	a (arcsec) (4)	b (arcsec) (5)	P.A. (deg) (6)	S_ν (mJy) (7)	SB[a] (8)	log P_ν[b] (9)	log $B_{\rm m.e.}$ (Gauss) (10)	log $P_{\rm m.e.}$ (dyne cm^{-2}) (11)	log $E_{\rm m.e.}$ (ergs) (12)
Natural-Weight Map											
RW-lobe-total	2.19	0.03	2.69	1.73	98	1.67	0.46	20.60	−4.60	−10.71	54.42
RW-1	2.00	0.17	1.09	0.69	38	0.52	0.88	20.09	−4.41	−10.32	53.62
RW-1a	1.87	0.28	0.51	0.47	125	0.19	1.03	19.65	−4.34	−10.19	53.09
RW-2	2.74	0.15	1.08	0.70	173	0.50	0.85	20.08	−4.41	−10.33	53.61
RW-2a	2.74	0.41	0.54	0.40	67	0.17	0.95	19.60	−4.33	−10.17	52.99
RW-bridge	1.23	−0.22	0.87	0.60	88	0.14	0.34	19.51	−4.51	−10.52	53.20
RW-jet	0.34	−0.04	0.77	0.67	15	1.31	3.26	20.49	−4.24	−9.99	53.77
Point core[c]	0.00	0.00	0.29	0.27	12	4.60	>74.80	21.04	>−3.74	>−8.99	< 53.56
RE-jet	−0.15	0.04	0.55	0.38	−2	0.28	1.64	19.83	−4.26	−10.02	53.10
RE-1	−1.04	0.18	1.23	0.89	123	0.39	0.45	19.97	−4.52	−10.55	53.66
RE-1a	−1.07	0.16	0.51	0.38	4	0.14	0.93	19.54	−4.33	−10.16	52.93
RE-2	−2.41	−0.38	1.38	0.71	99	0.12	0.16	19.45	−4.62	−10.75	53.31
Uniform-Weight Map											
RW-inner-jet	0.15	−0.01	0.33	0.30	21	1.40	18.91	20.52	−3.92	−9.35	53.34
RW-outer-jet	0.38	−0.12	0.23	0.18	59	0.17	5.87	19.61	−4.00	−9.52	52.58
RW-end-jet	0.49	−0.19	0.51	0.15	158	0.13	2.02	19.48	−4.11	−9.74	52.54
Point core[c]	0.00	0.00	0.16	0.15	10	3.80	>201.60	20.96	>−3.54	>−8.59	< 53.18
RE-inner-jet	−0.08	0.00	0.24	0.17	2	0.29	8.31	19.84	−3.95	−9.42	52.65
Deconvolved Uniform-Weight Map											
RW-inner-jet	0.14	0.00	0.29	0.13	89	1.76	58.88	20.62	−3.68	−8.86	53.05
RW-outer-jet	0.35	−0.08	0.28	0.11	56	0.29	11.37	19.84	−3.86	−9.23	52.52
RW-end-jet	0.49	−0.10	0.30	0.11	136	0.11	4.06	19.42	−3.99	−9.49	52.30

[a] Units of mJy arcsec^{-2}.
[b] Units of W Hz^{-1} Sr^{-1}.
[c] Aperture $\equiv$ beam FWHM.

may also play an important role in defining the location and shape of the innermost [O III] emission.

It is unclear whether the interaction at knot LW-1 merely disrupts the jet flow or completely destroys it. It is possible that the LW-1 cloud is sufficiently small that the flow envelops it and continues on to feed the western region, albeit less coherently. Alternatively, LW-1 may totally disrupt the jet, in which case the emission further to the west could arise from an earlier jet flow, before the LW-1 cloud entered the jet and blocked it. As we shall see in § 5.1, the Doppler velocity of the LW-1 cloud is close to systemic with low velocity dispersion, consistent with it having recently entered the flow and not yet begun to accelerate and break up under the impact of the jet.

In summary, it seems that the western nuclear radio jet runs into a compact cloud of ionized gas, spreading sideways and possibly distorting the cloud. The jet flow may either pass around the cloud or be destroyed by it; the interaction is probably sufficiently recent that it has neither accelerated nor broken up the cloud.

4.3. *Outer Western Lobe*

West of LW-1 the radio emission is weaker in RW-bridge, as one expects under either scenario just described—expansion following disruption, or absence of jet material downstream of its blockage. The radio emission is initially faint in the bridge area, but becomes brighter in knots RW-1a and -1b and RW-2a and -2b. Radio knot RW-1 falls mostly in a region of weak [O III], with some overlap between RW-1a and LW-3b. Knot RW-2 seems to straddle LW-5 but also extends north *outside* the [O III] region. The morphology of the [O III] knots suggests a dynamical interaction—all except LW-5 have upstream edge brightening and downstream flaring. Interestingly, however, the [O III] knot peaks are *not* in radio bright regions, preferring regions of low radio brightness.

We note that our description of this region is somewhat different from that of Capetti et al. (1996), who describe the [O III] distribution as surrounding the western radio component in a shell. As discussed in § 3.7, however, their choice of radio location was motivated in part to match the [O III] distribution and yield this "shell" effect. Our revised radio location and somewhat different radio lobe structure no longer gives this simple shell-like geometry, but instead suggests a more complex relation between optical and radio components.

Summarizing the possible physical phenomena encountered in the outer western lobe: the overall morphology suggests a disrupted flow filling a leaky bubble. Encounters with the flow may cause cloud compression on the upstream side and ablation on the downstream side.

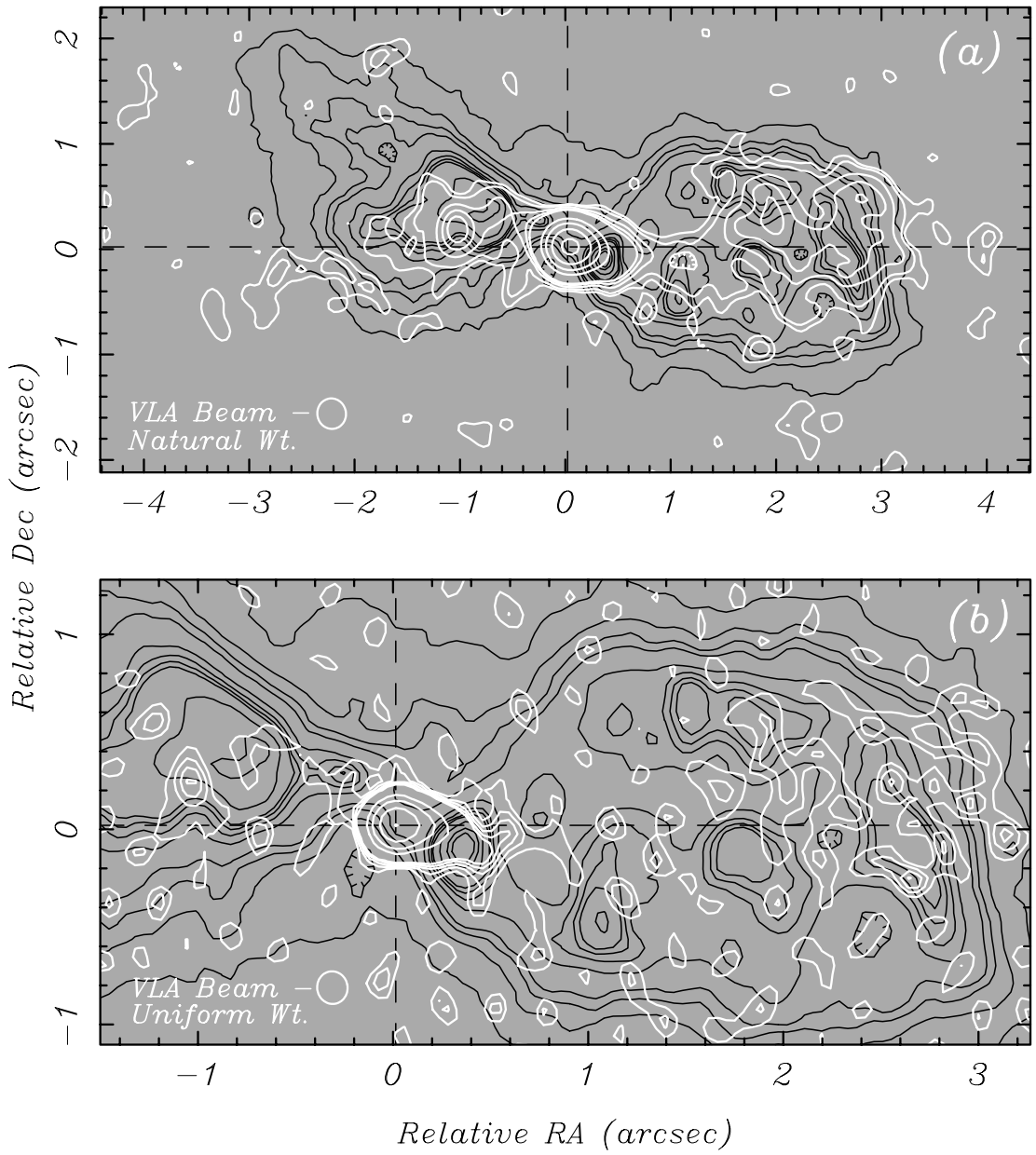

FIG. 9.—Comparison of radio structure (*white contours*) and [O III] image (*black contours*). Contour levels same as in Figs. 4 and 5*a*. (*a*) Natural-weight radio map showing larger scales. (*b*) Uniform-weight radio map showing inner regions at higher resolution. See § 3.7 for a discussion of the radio-optical registration and § 4 for a discussion of the relationship between the two components.

4.4. *Eastern Fan*

While significantly weaker than the western radio jet, the inner eastern radio structure shows similar characteristics. The RE-bridge points directly at the brightest [O III] emission, and the radio component RE-1b sits right on top of the [O III] double knot LE-1a and 1b. There seems little doubt that the eastern jet flow strikes, ablates, and accelerates the [O III] cloud LE-1: the line emission is brightened on the side facing the nucleus; it spreads away from the nucleus in a fan shape; there are velocities of roughly +700 km s^{-1} (Whittle et al. 1988; Pedlar et al. 1989). The brightest part forms two ridges running down the inner fan. It is possible that these ridges are formed by the expanding sides of a channel created by part of the jet material as it burrows into the cloud complex. Indeed, as discussed in § 5.1, the FOS aperture (Ap 9) that samples this region shows a double profile, consistent with lateral expansion around a jet. At this point (RE-1b), the radio source is deflected by $\sim 45^\circ$ and continues along P.A. $\sim 120^\circ$ via component RE-1a toward RE-2. Unlike the western knot LW-1, it seems the eastern [O III] cloud complex LE-1 deflects rather than destroys the jet flow. One might even speculate that the deflected jet flow continues to interact down the southern ridge of the fan, giving rise to its wavy appearance. As with the western lobe, there are large-scale similarities and small-scale differences in the [O III] and radio distributions. The similarities include superposition of RE-1b and LE-1a and -1b; approximate coincidence of the region surrounding RE-1 and LE-ifan; and the match between the ridge of radio emission along position angle 120° and the southern boundary of the [O III] fan. Anticorrelations include: the brightest radio component, RE-1a, falls off the edge of the brightest [O III] region in a local

minimum; several weak radio features at the edge of the RE-1 lobe fall in regions of weak [O III] emission and/or skirt an [O III] edge; and the west side of RE-2 flanks the southeast rim of the [O III] fan (some of these are best seen using the highest resolution FOC data). As with the western lobe, then, globally there is a close relation between the jet flow and line-emitting components, but locally these components do not seem to mix efficiently.

The northern arm of the eastern fan may be interestingly different. It is long ($\sim 3''$), straight, shows no signs of corrugation, has no associated radio emission, and seems to have quiescent kinematics (as found in the ground-based spectroscopy of Pedlar et al. 1989). It seems quite likely that this gas is undisturbed by the radio flow, and its overall geometry stems from illumination effects, not ablation. The obvious candidate for the ionizing source is the nucleus located behind the dust lane—indeed, the apex of both the inner fan and the outer fan are close to the radio nucleus behind the dust lane.

In summarizing the physical processes occurring on the eastern side, we find many of those noted for the western side: strong first jet encounter, deflection, gas acceleration, and a lack of intermixing between radio jet flow and line-emitting materials. There are, however, important differences from the western side: the jet does not seem to inflate a (leaky) bubble, but instead appears to be completely deflected by the initial cloud collision. The initial encounter may be more damaging to the cloud, with possible penetration along a channel, driving a lateral expansion. Finally, the overall geometry of this side may owe more to a conical UV radiation field from the nucleus than the effects of hydrodynamic interactions.

5. IONIZED GAS KINEMATICS

Whittle et al. (1988) and Pedlar et al. (1989) present high-resolution ground-based spectra of Mrk 78 showing four kinematic components: a galactic scale rotating component, a kinematically quiet extended narrow-line region, a near-nuclear highly redshifted eastern component, and a near-nuclear highly blueshifted western component. While these ground-based data reveal the *presence* of jet-accelerated gas, they do not clearly reveal the *nature* of the interaction. Our FOS data help considerably in this regard, although we must wait for the fuller spatial coverage of STIS to construct a comprehensive picture of the flow patterns.

Defining the absolute velocity scale of our FOS spectra requires four corrections—a zero-point offset from our wavelength calibration exposure (+230 km s^{-1}), a conversion from vacuum to air (-86 km s^{-1}), a correction to heliocentric (-22 km s^{-1}), and an aperture-dependent correction, resulting from the nonuniform aperture illumination (in the range ± 45 km s^{-1}, calculated by projecting the emission distribution within each aperture along the dispersion direction). The final velocity scale was confirmed, at least for Ap-9, by comparing with ground-based spectra—the narrow redshifted component agrees to within ~ 20 km s^{-1}.

Figure 10 shows the [O III] λ5007 profiles for all 10 FOS apertures. The vertical line indicates systemic velocity (11,052 km s^{-1}, taken from the emission-line rotation curve in Whittle et al. 1988), while the tick marks and dotted lines indicate ± 1000 km s^{-1} offsets. Rather than discuss each aperture separately, we group them to emphasize specific physical processes. When given, values of FWHM are corrected for resolution by quadrature subtraction of the FOS instrument FWHM of 320 km s^{-1}.

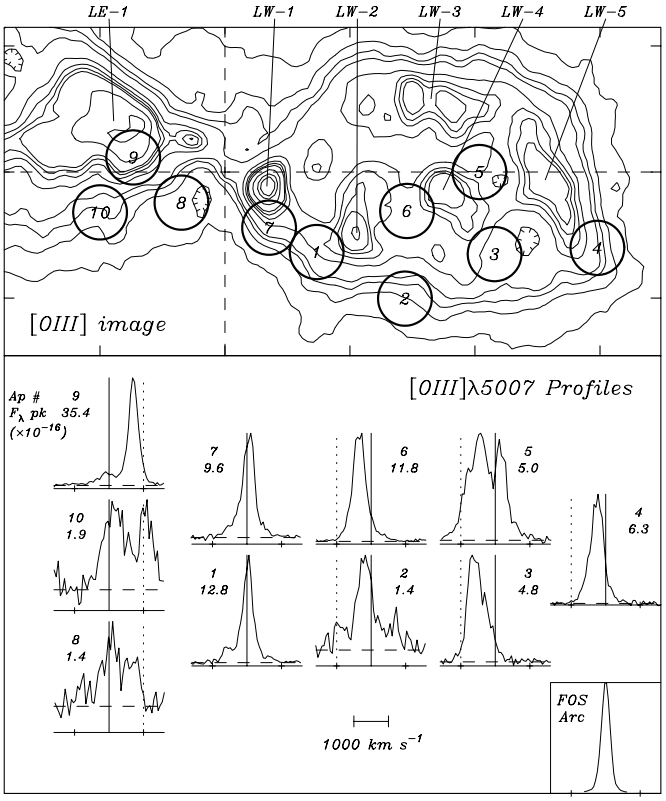

FIG. 10.—*Top*: Contours of [O III] line emission taken from the PC image (tick marks denote arcseconds) with 10 FOS apertures superposed. *Bottom*: [O III] λ5007 emission-line profiles from the 10 FOS apertures. Dashed horizontal lines mark the continuum level; solid vertical lines mark systemic velocity (11,052 km s^{-1} heliocentric); dotted vertical lines and tick marks on the baseline mark 1000 km s^{-1} velocity offsets from systemic. Aperture number and peak flux (in units of 10^{-16} ergs s^{-1} cm^{-2} Å^{-1}) are marked by each profile. The FOS instrument profile (taken from a wavelength calibration exposure) is shown at bottom right.

5.1. *Jet Impact on LE-1*

Ap-9 samples the inner edge of the bright knot LE-1, yielding an [O III] profile dominated by a strong narrow component that is highly redshifted (+700 km s^{-1}), together with a much weaker slightly blueshifted component (-70 km s^{-1}). Clearly, at the site of the primary jet interaction the gas has been rapidly accelerated to high velocity. From the current data alone, it is unclear how to interpret the double [O III] profile—either the two components are unrelated, with the weaker one coming from unperturbed gas near systemic velocity, or both components might arise from gas driven laterally away from the jet.[5] In this case, one might also interpret the two ridges of emission at LE-1a and -1b as arising from gas compressed by the lateral expansion. Interestingly, the redshifted component is essentially *unresolved* (FWHM ≤ 200 km s^{-1}), indicating that the acceleration mechanism, whatever it is, is highly coherent and introduces little internal turbulence.

One consequence of the interaction at LE-1 is that the radio jet is deflected (Fig. 9). Note, however, that despite this deflection and the possibly related dramatic acceleration of line-emitting gas, the radio luminosity is not significantly enhanced

[5] Recent STIS data confirm widespread split lines over LE-1, supporting the possibility of lateral expansion.

at the site of the interaction—both RE-bridge and RE-1b are quite weak near LE-1. As with the western interaction at LW-1, these strong interactions do not seem to reenergize the radio source.

Downstream from this primary interaction at LE-1, Ap-10 shows further gas acceleration with a component at redshift +1090 km s^{-1}. Since this aperture samples the "wavy" southern boundary to the [O III] fan, the high gas velocity supports the overall picture of accelerated ablata driven away from the primary jet-cloud interaction by the jet flow. These high velocities do, of course, provide a lower limit to the jet flow speed of $\geq$1100 km s^{-1}.

5.2. *Dust Lane*

Ap-8 falls pretty much within the central obscuring dust lane and consequently has very weak emission. There is an approximately zero-velocity component that seems quite broad, although the feature at roughly +625 km s^{-1} may arise from light scattered into the aperture from the very bright nearby knot LE-1 (sampled more completely by Ap-9).

5.3. *Jet Impact on LW-1*

The kinematic signature of the jet impact on LW-1 is *quite different* from that for LE-1. The [O III] profile from Ap-7 is close to zero velocity (roughly +50 km s^{-1}) and quite narrow (FWHM $\sim$ 300 km s^{-1}). Despite the fact that this knot appears to take the brunt of the western jet interaction (see Fig. 9*b*), there has been little discernible bulk acceleration. One might be concerned that Ap-7 samples only the southern edge of the [O III] knot, but ground-based spectra dominated by the emission from LW-1 show the same strong narrow component at approximately zero velocity (roughly -60 km s^{-1}). The absence of high velocities may be related to the details of the jet-cloud interaction—the cloud does not fully impede the jet (see § 4.2), and its compactness may indicate a recent entry into the jet flow, possibly brought in by galactic rotation, with insufficient time to accelerate significantly. This contrasts with the eastern knot and inner fan, which shows much clearer signs of long-term interaction. There is nevertheless weak evidence for gas acceleration—the [O III] profile is asymmetric with a blue wing which extends to roughly -950 km s^{-1}, possibly arising from ablata driven off the [O III] knot toward the south.

5.4. *Velocities Outside the Flow*

From Figure 9*a*, it seems that the radio jet coincides with LW-1 and passes just north of LW-2, and so the FOS apertures 7, 1, and 2 all seem to lie to the south of the main flow zone. Not surprisingly, therefore, their [O III] profiles are all quite narrow and close to zero velocity, with a marginal velocity gradient between Ap-7 and Ap-1 (+50 to +20 km s^{-1}), picking up to -180 km s^{-1} at Ap-2. There may be a hint of more accelerated gas in the blue wing of Ap-1 at -540 km s^{-1}, possibly a continuation of the blue wing gas seen in Ap-7 near knot LW-1.

5.5. *Velocities Within the Flow*

FOS apertures 6, 5, and 3 all lie within the main western lobe. From the radio and [O III] images alone, it is very difficult to say where the radio jet goes after its interaction at LW-1. It does seem likely, however, that at least some part of the disrupted flow continues through the outer western lobe, possibly ultimately escaping the region through gaps between the emission clouds. The [O III] kinematics are consistent with this picture. Within Ap-6 the gas has been significantly accelerated relative to the upstream apertures Ap-7 and Ap-1, with velocity roughly -350 km s^{-1} and FWHM $\sim$ 300 km s^{-1}. Further into the lobe, at Ap-5, the bulk velocity (-475 km s^{-1}) and velocity dispersion (FWHM $\sim$ 790 km s^{-1}) increase. In this aperture, there is an additional [O III] component at mild *positive* velocity (+200 km s^{-1}), suggesting that the overall dynamics of the lobe may not be simply outward motion from the nucleus, but also outward away from the lobe axis—as one would expect for an expanding leaky bubble. The highest velocities are found in Ap-3, with a component at -610 km s^{-1} with FWHM $\sim$ 500 km s^{-1}. This supports the possibility that part of the flow emerges between LW-4 and LW-5, in what one might call a "blow-out zone."

5.6. *Outer Edge of the Western Lobe*

Ap-4 is located on the outer edge of the western lobe, at the southern tip of knot LW-5 and at the edge of the blow-out zone. Not surprisingly, the peak velocity is closer to systemic, at roughly -240 km s^{-1}, than are the velocities within the western lobe. The profile is moderately narrow (FWHM $\sim$ 230 km s^{-1}) but has wings extending from -900 to +350 km s^{-1}. It appears that this outer region is beginning to be disturbed by the advancing lobe.

We note here that the FOS data are all consistent with the ground-based data presented in Whittle et al. and Pedlar et al. In particular, the blueshifted component peaks in strength around the middle of the lobe ($\sim$1.″90 west), has a large line width (FWHM $\sim$ 450 km s^{-1}), and has a mean velocity roughly -480 km s^{-1} at the lobe center, decreasing somewhat toward the outer edge of the lobe.

5.7. *Normally Rotating Component*

Ground-based data indicates a fairly clear rotating component, starting at roughly +140 km s^{-1} $\sim$5″ east, dropping across systemic velocity within $\sim$2″ of the nucleus, and emerging at roughly -140 km s^{-1} on the western side. While present in some of the FOS data, this rotating component is less easily identified. It is probably the weak component near zero velocity seen in Aps 8, 9, and 10, consistent with undisturbed gas lying above or below the main jet driven gas. Just west of the nucleus in Aps 7 and 1, it is difficult to track the rotating component because knot LW-1 has approximately zero velocity. Indeed, it now seems that this knot component was included as part of the ambient rotation in the ground-based analyses, when perhaps it should not have been. In the rest of the western apertures, Aps 2, 3, 4, 5, and 6, there is no clear signature of a near–zero-velocity component. The emission seen in the ground-based data may either have come from further north (the FOS apertures tend to lie on the south side of the lobe) and/or from further west.

In summary, several interesting kinematic phenomena are suggested. (1) Following jet interaction and deflection, gas can be accelerated to high velocities with little generation of velocity dispersion (Ap-9 on LE-1). (2) Gas ablated away from the main cloud continues to be accelerated (Ap-10). (3) A bright cloud in the jet flow can also show *little or no* bulk acceleration, implying that fast shocks may not be important in ionizing the gas (Ap-7 on LW-1). (4) Outside the jet flows, the gas remains relatively quiescent (Aps 1 and 2). (5) As a jet flow progresses through a complex lobe, accelerations continue to grow (Aps 6, 5, and 3). (6) The highest gas velocities

may occur at points where the jet flow breaks out of the growing "bubble" in a blow-out zone (Ap-3). (7) At the leading edge of the advancing bubble/lobe, gas velocities are intermediate between the external ambient gas and the internal lobe gas (Ap-4).

6. SUMMARY AND CONCLUSIONS

This is the first part of a study of jet-gas interactions in the Seyfert 2 galaxy Mrk 78. Here we present the basic imaging and FOS data, comparing the emission-line and radio morphologies and a preliminary study of the emission-line kinematics. Our intention is to construct a fairly detailed phenomenological description of the interaction between the expanding radio source and the surrounding line-emitting gas, aiming to identify the important physical processes. In companion papers, we consider in more detail the ionization conditions in the line-emitting gas, the distribution and exchange of energy among the various components, the nature of the jet flow, and the origin of the extended blue continuum light.

Our data provide high-quality [O III] emission-line and 3.6 cm radio images, as well as intermediate-resolution spectra from 10 locations. Data from the *HST* archive yield additional *V*, *U*, and [O II] images. A careful comparison of all these indicates a number of important physical processes, which we now summarize and discuss.

1. *The overall context is probably a post merger remnant*.—A tilted nuclear dust lane lies within a rather featureless early type galaxy with a highly extended and asymmetric gas distribution. Astrometric registration places the radio nucleus close to a compact feature within the dust lane, which is probably the true, although heavily obscured, optical nucleus.

2. *Both nuclear photoionization and hydrodynamic interactions play a role in determining the overall emission-line geometry*.—At faint levels, the more extended [O III] emission has nucleocentric conical form aligned within a few degrees of the very innermost radio axis (P.A. $\sim 90^\circ - 270^\circ$, $R \lesssim 0\farcs2$), which we presume to be the axis of the nuclear ionizing radiation field. However, at high flux levels closer to the nucleus the [O III] emission is oriented differently, aligned and cospatial with the ends of the emergent radio jet, which has P.A. $\sim 70^\circ$–240° on scales $\sim 0\farcs2 - 0\farcs6$. At intermediate flux levels, aspects of both orientations can be found.

3. *Radio jet flows can be deflected and disrupted in their interaction with line-emitting gas*.—Mrk 78 provides two clear examples. Close to the innermost [O III] western knot (LW-1), the radio jet ends in an abrupt dog leg (Figs. 5 and 9). Immediately beyond this point the radio emission is weak, so it appears that the flow is badly disrupted by the interaction. On the eastern side, the radio source emerges at P.A. $\sim 90^\circ$, quickly turns to P.A. $\sim 70^\circ$, but clearly changes to P.A. $\sim 120^\circ$ after encountering (and accelerating) the luminous [O III] knot LE-1. In this case, the interaction seems to redirect, rather than disrupt, the radio source. The relevant difference between the two sides may be the size and/or velocity of the blocking gas clouds (LE-1 is much more extensive than LW-1 and has already been accelerated to high velocity).

4. *Strong jet-gas interactions need not enhance the radio emission*.—At both LE-1 and LW-1, where the jet flow seems most seriously changed, the radio emission is not significantly enhanced. Indeed, these interaction regions mark the end of the inner radio jet and are weaker than nearby emission. This is puzzling: even if jet shocks are absent, one expects compression alone to amplify any magnetic fields and hence radio emissivity.

5. *Radio source material and line-emitting gas do not easily interpenetrate*.—In a sense, the jet disruptions and deflections at LW-1 and LE-1 already indicate the inability of the radio source material to penetrate the line-emitting gas. However, elsewhere in the region there is significant evidence for an anticorrelation between radio emission and line emission. The western radio components tend to fall between the [O III] knots, while on the eastern side the radio source flanks the [O III] fan with components lying in local [O III] minima. This phenomena has, of course, been noted before, both for Seyferts (e.g., Falcke et al. 1998) and radio galaxies (e.g., Heckman et al. 1982). Apart from the physical reason that prevents intermingling (e.g., magnetic or density barriers), this observation also indicates how the radio source might advance through an emission-line region—either it flows along lines of least resistance between the [O III] knots and/or it sweeps up gas as it flows in a snowplow effect, possibly creating the [O III] knots or shells in this way. In Mrk 78, the fact that the [O III] gas can both deflect and be accelerated by the radio source suggests that the mode in which the radio source expands may lie between the two situations just described—depending on the geometry, the [O III] gas may channel the radio source and/or be swept along by it.

6. *The radio source can ablate and distort the line-emitting gas*.—There are several indications that the [O III] gas distribution has been modified by the radio source. The large fanlike [O III] complex (LE-1) has an apex close to the end of the eastern radio jet, and a corrugated southern boundary next to the deflected radio source. A number of the [O III] knots on the western side appear sharp upstream and flare downstream, including the innermost bright knot LW-1. Although some of these effects may be related to central source photoionization, when coupled with the kinematic evidence it seems clear that the radio source can deform and ablate [O III]-emitting gas.

7. *Line-emitting gas can be accelerated coherently to high velocities by the radio source*.—The FOS aperture over LE-1 (Ap 9) shows an [O III] profile with a strong narrow core centered at +700 km s^{-1}. Since this aperture is located at the upstream edge of the [O III] knot, where the jet first encounters it, the [O III] gas has clearly experienced bulk acceleration by $\sim$700 km s^{-1} within a few hundred parsecs. The fact that the profile is so *narrow* (essentially unresolved by the FOS) places strong constraints on the acceleration mechanism—it cannot introduce turbulence and/or it must act uniformly and coherently on the gas.

8. *A jet collision with a gas cloud need not accelerate or ionize it*.—In a second region of strong jet-gas interaction (LW-1), the kinematic signature is completely different. Remarkably, the [O III] profile shows almost no kinematic response to the jet impact—the line is near systemic velocity and has only modest width. Perhaps the interaction is too recent, the geometry unfavorable, or the mass too great.

9. *Kinematic evidence supports jet driven flows across the western emission region*.—Although the spatial coverage is not ideal, seven apertures sample the western region, showing a wide range of [O III] velocities. Roughly speaking, the more central is the aperture in the western lobe the higher the blueshift: along the southern rim (Aps 1 and 2) the velocities are only 0 to -200 km s^{-1}, while within the knotted region (Aps 5 and 6) they have increased to -350 to -450 km s^{-1}. Mostly, the profiles are single peaked ruling out a simple

expanding shell, although in places (Ap-5) two components are seen showing that more complex (lateral?) flow patterns can occur. Overall, the kinematics support a picture in which the radio flow moves between and around ionized gas and accelerates it, more so near the lobe's center and less so at the edges. Two special cases (Aps 4 and 3) deserve further comment:

10. *At the leading edge, the velocities can be low.*—Ap-4 samples the leading boundary of the western lobe, where one might expect an initial encounter with the ambient medium to be occurring. Rather than finding high velocities associated with a bow shock, the velocities are instead modest (-240 km s^{-1}) suggesting a weak kinematic interaction. This is, perhaps, not surprising since the radio image indicates FR I rather than FR II morphology, lacking the clear signature of an edge-brightened lobe. This region *may not*, therefore, conform to one of the standard descriptions of radio source interaction in Seyfert galaxies, in which ambient gas is compressed and accelerated by a leading bow shock, becoming visible as line-emitting gas as it cools behind the shock (e.g., Taylor, Dyson, & Axon 1992).

11. *The radio source can break out of a region, sweeping line-emitting gas at high velocity.*—Ap-3 samples a region where [O III] and radio morphology suggest a possible lateral "breakout" of the radio source (between LW-4 and LW-5). Consistent with this, the [O III] line profile at this point shows the highest velocities seen on the western side (-600 km s^{-1}). While somewhat speculative, it seems that radio source development not only includes flows within the line-emitting region, but also includes the leakage or breakout of those flows as they exit the region. In doing so, the radio source carries line-emitting material at high velocity.

12. *Geometry and kinematics provide simple constraints on the radio jet velocity.*—Since the western gas is blueshifted, we know the western radio jet is approaching. This is at least consistent with relativistic beaming as a source of the asymmetry in the strength of the innermost radio jet, in which the western side is the brighter. For the flux ratio of $\sim$5 and jet angles of 30°–60° (basically excluding pole-on and edge-on orientations, given the line-emitting geometry and velocities) yields an upper limit of ~ 0.3–$0.5c$ for the jet speed. Obviously, a lower limit to the jet speed comes from the maximum observed [O III] velocity, $\sim$1100 km s^{-1}, which is found in the redshifted component of Ap-10, just downstream of the main interaction occurring at LE-1.

We briefly bring these results into a single framework. First, we note that the morphological and kinematic patterns do not support any of the idealized theoretical models most frequently discussed, at least in their pure form. These models include (1) an expanding plasmon compressing and shocking ambient gas (Pedlar, Dyson, & Unger 1985); (2) a jet-driven bow shock with line-emitting gas emerging within the post-shock cooling region (e.g., Taylor et al. 1992; Ferruit et al. 1997; Bicknell, Dopita, & O'Dea 1997); (3) gas that is laterally entrained and accelerated along the jet length (e.g., Blandford & Konigl 1979; Bicknell 1986; Fedorenko, Paltani, & Zentsova 1996); and (4) gas that is driven away from the jet axis by an expanding cocoon (e.g., Steffen et al. 1997; Lim & Steffen 2001). Although local versions of phenomena described in these models may well be occurring, the global pattern that they suggest is missing—the observed regions are simply too complex. Not least, there appear to be significant differences between the east and west side even in this one object. Instead, we have attempted a phenomonological description based on the observed morphological and kinematic patterns. The western side seems best described overall as a leaky bubble; the radio flow enters the region after a disruptive encounter with a compact cloud, moves predominantly between the ionized gas knots accelerating and ablating them in the process, and finally exits the region through blow out gaps. In contrast, the eastern side seems best described overall as a head-on deflecting encounter between the jet flow and a complex region, with significant gas acceleration and ablation.

As a final suggestion, we note that a possible evolutionary sequence for jet-gas interactions may be directly visible in Mrk 78. The sequence of "initial," "intermediate," and "late" stages can be seen at LW-1, LE-ifan, and the western lobe complex, respectively. At the initial stage, a dense (molecular?) cloud enters the inner jet flow, perhaps brought in by galactic rotation. The light jet is thoroughly disrupted by this dense obstacle without significantly distorting or accelerating it. This is the situation we find at LW-1. After some time, the jet begins to disrupt, ablate, and accelerate the gas, either downstream or laterally as the jet drives a channel into the cloud complex. As the region changes, the affect on the jet flow may be less severe, causing deflection rather than disruption. This is the situation we find at LE-ifan. As more time passes, this region begins to break up into a number of knots under the continued influence of the radio flow, separating into a larger region with channels and gaps through which the radio source penetrates. This is the situation we find in the western lobe complex. Ultimately, either the gas knots disperse under the continued influence of the radio source, or a new cloud complex enters the jet region near the nucleus, blocking the jet flow to the outer older region. This changeover process may be occurring on the western side in Mrk 78, where LW-1 is currently taking the brunt of the jet flow, while the outer region is close to dispersing. Under this scheme, a rough estimate for the evolutionary timescale is a few times 10^6 yr (simply the time to cross the western lobe, $\sim$2 kpc, moving at speeds found in LE-ifan, $\sim$700 km s^{-1}). If the longevity of the nuclear activity is associated with the settling time for the nuclear gas/dust disk, then the sequence described above may happen many times during the active phase. It is even possible that the more extended line emission seen on both sides has originated in earlier episodes of jet driven expulsion.

It is a pleasure to thank Geoff Bicknell, Mike Dopita, Mark Allan, Charlie Nelson, John Silverman, David Rosario, Joss Bland-Hawthorn, and Dave De Young for stimulating discussions. We thank Alissandro Capetti for providing his reduced pre-COSTAR FOC images, and Anuradha Koratka, Steve Bergeron, Nick White, and Mike Hsu for advice during the data reduction. M. W. thanks Inter University Center for Astronomy and Astrophysics, the Mount Stromlo and Siding Springs Observatory, the Anglo-Australian Observatory, and the Australian National Telescope Facility, for hospitality while some of this work was being done. Support for proposal numbers GO 2493 and GO 5417 was provided by NASA through a grant from the Space Telescope Science Institute, which is operated by the Association of Universities for Research in Astronomy, Inc., under NASA contract NAS 5-26555. This research was also supported by the National Science Foundation through grant AST 95-27289.

REFERENCES

Adams, T. F. 1973, ApJ, 179, 417
Axon, D. J., Capetti, A., Fanti, R., Morganti, R., Robinson, A., & Spencer, R. 2000, AJ, 120, 2284
Axon, D. J., Marconi, A., Maccheto, F. D., Schreier, E., & Robinson, A. 1998, ApJ, 496, L75
Baum, S. A., Heckman, T. M., & van Breugel, W. J. M. 1992, ApJ, 389, 208
Best, P. N., Inskip, K. J., Röttgering, H. J. A., & Longair, M. S. 2002, Emission Lines from Jet Flows, ed. W. J. Henney, W. Steffen, A. C. Raga, & L. Binette (Rev. Mexicana Astron. Astrofis. Ser. Conf. 13) (Mexico, D.F.: Inst. Astron. Univ. Nac. Autonoma México), 155
Best, P. N., Röttgering, H. J. A., & Longair, M. S. 2000, MNRAS, 311, 23
Blandford, R. D., & Konigl, A. 1979, Astrophys. Lett., 20, 15
Bicknell, G. V. 1986, ApJ, 305, 109
Bicknell, G. V., Dopita, M. A., & O'Dea, C. P. O. 1997, ApJ, 485, 112
Bower, G., Wilson, A. S., Mulchaey, J., Miley, G. K., Heckman, T. M., & Krolik, J. H. 1994, AJ, 107, 1686
Capetti, A. 2002, Emission Lines from Jet Flows, ed. W. J. Henney, W. Steffen, A. C. Raga, & L. Binette (Rev. Mexicana Astron. Astrofis. Ser. Conf. 13) (Mexico, D.F.: Inst. Astron. Univ. Nac. Autonoma México), 163
Capetti, A., Axon, D. J., Macchetto, F. D., Marconi, A., & Winge, C. 1999, ApJ, 516, 187
Capetti, A., Axon, D. J., Macchetto, F. D., Sparks, W. B., & Boksenberg, A. 1996, ApJ, 469, 554
Capetti, A., Macchetto, F., Sparks, W. B., & Boksenberg, A. 1994, ApJ, 421, 87
Cecil, G. 1988, ApJ, 329, 38
Cecil, G., Dopita, M. A., Groves, B., Wilson, A. S., Ferruit, P., Pécontal, E., & Binette, L. 2002, ApJ, 568, 627
Cecil, G., et al. 2000, ApJ, 536, 675
Clark, N. E., Axon, D. J., Tadhunter, C. N., Robinson, A., & O'Brien, P. 1998, ApJ, 494, 546
Clements, E. 1981, MNRAS, 197, 829
Cooke, A. J., Baldwin, J. A., Ferland, G. J., Netzer, H., & Wilson, A. S. 2000, ApJS, 129, 517
de Bruyn, A. G., & Sargent, W. L. W. 1978, AJ, 83, 1257
de Bruyn, A. G., & Wilson, A. S. 1978, A&A, 64, 433
DeRobertis, M. M. 1987, ApJ, 316, 597
De Vries, W. H., O'Dea, C. P., Baum, S. A., & Bartel, P. D. 1999, ApJ, 526, 27
Dopita, M. A., & Sutherland, R. S. 1995, ApJ, 455, 468
———. 1996, ApJS, 102, 161
Falcke, H., Wilson, A. S., & Simpson, C. 1998, ApJ, 502, 199
Fedorenko, V. N., Paltani, S., & Zentsova, A. S. 1996, A&A, 314, 368
Ferland, G. J., & Osterbrock, D. E. 1986, ApJ, 300, 658
Ferruit, P. 2002, Emission Lines from Jet Flows, ed. W. J. Henney, W. Steffen, A. C. Raga, & L. Binette (Rev. Mexicana Astron. Astrofis. Ser. Conf. 13) (Mexico, D.F.: Inst. Astron. Univ. Nac. Autonoma México), 183
Ferruit, P., Binette, L., Sutherland, R. S., & Pécontal, E. 1997, A&A, 322, 73
Ferruit, P., Wilson, A. S., Falcke, H., Simpson, C., Pécontal, E., & Durret, F. 1999, MNRAS, 309, 1
Gallimore, J. F., Baum, S. A., & O'Dea, C. P. 1996, ApJ, 464, 198
Gelderman, R., & Whittle, M. 1994, ApJS, 91, 491
Haniff, C. A., Wilson, A. S., & Ward, M. J. 1988, ApJ, 334, 104
Heckman, T. M., Miley, G. K., Balick, B., van Breugel, W. J. M., & Butcher, H. R. 1982, ApJ, 262, 529
Heckman, T. M., Miley, G. K., van Breugel, W. J. M., & Butcher, H. R. 1981, ApJ, 247, 403
Kennicutt, R. C. 1992, ApJ, 388, 310
Lim, A. J., & Steffen, W. 2001, MNRAS, 322, 166
Lucy, L. B. 1974, AJ, 79, 745
Miley, G. K. 1980, ARA&A, 18, 165
Mulchaey, J. S., Wilson, A. S., Bower, G. A., Heckman, T. M., Krolik, J. H., & Miley, G. K. 1994, ApJ, 433, 625
Mullis, C. 1994, Senior thesis, Univ. Virginia
Nelson, C. H., & Whittle, M. 1995, ApJS, 99, 67
———. 1996, ApJ, 465, 96
Pedlar, A., Dyson, J. E., & Unger, S. W. 1985, MNRAS, 214, 463
Pedlar, A., Meaburn, J., Axon, D. J., Unger, S. W., Whittle, M., Meurs, E. J. A., Guerrine, N., & Ward, M. J. 1989, MNRAS, 238, 863
Sargent, W. L. W. 1972, ApJ, 173, 7
Schmitt, H. R., Donley, J. L., Antonucci, R. R. J., Hutchings, J. B., Kinney, A. L., & Pringle, J. E. 2003, ApJ, 597, 768
Steffen, W., Gomez, J. L., Williams, R. J. R., Raga, A. C., & Pedlar, A. 1997, MNRAS, 286, 1032
Tadhunter, C. N. 2002, Emission Lines from Jet Flows, ed. W. J. Henney, W. Steffen, A. C. Raga, & L. Binette (Rev. Mexicana Astron. Astrofis. Ser. Conf. 13) (Mexico, D.F.: Inst. Astron. Univ. Nac. Autonoma México), 213
Tadhunter, C. N., Villar-Martin, M., Morganti, R., Bland-Hawthorn, J., & Axon, D. J. 2000, MNRAS, 314, 849
Taylor, D., Dyson, J. E., & Axon, D. J. 1992, MNRAS, 255, 351
Ulvestad, J. S., Wilson, A. S., & Sramek, R. A. 1981, ApJ, 247, 419
Unger, S. W., Pedlar, A., Axon, D. J., Whittle, M., Meurs, E. J. A., & Ward, M. J. 1987, MNRAS, 228, 671
Veilleux, S., & Bland-Hawthorn, J. 1997, ApJ, 479, L105
Veilleux, S., Bland-Hawthorn, J., Cecil, G., Tully, R. B., & Miller, S. T. 1999, ApJ, 520, 111
Veilleux, S., Cecil, G., Bland-Hawthorn, J., & Shopbell, P. L. 2002, Emission Lines from Jet Flows, ed. W. J. Henney, W. Steffen, A. C. Raga, & L. Binette (Rev. Mexicana Astron. Astrofis. Ser. Conf. 13) (Mexico, D.F.: Inst. Astron. Univ. Nac. Autonoma México), 222
Whittle, M. 1985a, MNRAS, 213, 1
———. 1985b, MNRAS, 213, 33
———. 1992a, ApJS, 79, 49
———. 1992b, ApJ, 387, 109
———. 1992c, ApJ, 387, 121
Whittle, M., Pedlar, A., Meurs, E. J. A., Unger, S. W., Axon, D. J., & Ward, M. J. 1988, ApJ, 326, 125
Wilson, A. S. 1982, in IAU Symp. 97, Extragalactic Radio Sources, ed. D. S. Heeschen & C. M. Wade (Dordrecht: Reidel), 179
Wilson, A. S., & Heckman, T. M. 1985, in Astrophysics of Active Galaxies and Quasi-Stellar Objects (Mill Valley: Univ. Sci.), 39
Wilson, A. S., & Willis, A. G. 1980, ApJ, 240, 429